ADAPTIVE CONTROL
FOR MARS ATMOSPHERIC FLIGHT

A Thesis

by

CAROLINA ISABEL RESTREPO

Submitted to the Office of Graduate Studies of
Texas A&M University
in partial fulfillment of the requirements for the degree of

MASTER OF SCIENCE

August 2007

Major Subject: Aerospace Engineering

ADAPTIVE CONTROL
FOR MARS ATMOSPHERIC FLIGHT

A Thesis

by

CAROLINA ISABEL RESTREPO

Submitted to the Office of Graduate Studies of
Texas A&M University
in partial fulfillment of the requirements for the degree of

MASTER OF SCIENCE

Approved by:

Chair of Committee,	John Valasek
Committee Members,	John Hurtado
	John Junkins
	William Schneider
Head of Department,	Helen Reed

August 2007

Major Subject: Aerospace Engineering

ABSTRACT

Adaptive Control
for Mars Atmospheric Flight. (August 2007)
Carolina Isabel Restrepo, B.S. Texas A&M University
Chair of Advisory Committee: Dr. John Valasek

The new vision for space exploration will focus on sending humans to the moon and eventually to Mars. This endeavor presents new challenges that are critically different from the past experience with robotic missions to Mars. For example, the strict landing accuracy requirements for a manned space vehicle make it necessary to fly a controlled entry trajectory rather than a more robust ballistic entry trajectory used for some robotic missions. The large variations in Mars atmospheric properties make a controlled entry and a safe precision landing for manned missions a difficult engineering problem. Model reference adaptive control is a candidate solution for the Mars entry control problem. This type of controller has an adaptation mechanism that reduces tracking errors in the presence of uncertain parameters such as atmospheric density or vehicle properties. This thesis develops two different adaptive control systems for the Mars ellipsled, a vehicle which is much larger than those that carried robotic payloads to Mars in the past. A sample mission will have multiple ellipsleds arriving at Mars carrying an assortment of payloads. It is of critical importance that the vehicles land in close proximity to each other to best assure that the crew has manageable access to their payloads.

The scope of this research encompasses the atmospheric flight of the ellipsled, starting at the entry interface point through the final parachute deployment. Tracking performance of an adaptive controller for prescribed entry trajectories in the presence of atmospheric and vehicle model uncertainties is shown here. Both adaptive

controllers studied in this thesis demonstrate successful adaptation to uncertainties in the Martian atmosphere as well as errors in the vehicle properties. Based on these results, adaptive control is a potential option for controlling Mars entry vehicles.

Para Tito

Gracias por creer en mí desde el principio.

Te prometo que apenas pueda, te llevo a la luna.

ACKNOWLEDGMENTS

I would like to thank Dr. John Valasek for being so much more than a graduate advisor. He has been a source of encouragement and inspiration since my undergraduate years at Texas A&M. I am most grateful for his belief in me and will always remember his genuine enthusiasm for helping me reach my academic and career goals.

I would also like to thank my committee members Dr. John Junkins, Dr. John Hurtado, and Dr. Bill Schneider for their valuable contributions to my research. Dr. Hurtado and Dr. Junkins both shared their knowledge of dynamics in and out of the classroom, as well as provided valuable insight on this research. I would like to thank Dr. Schneider for his optimism and support during my time as a graduate student. All of my committee members have been great examples of what I can achieve with hard work and dedication.

This research was also possible because I have had the support of the Aeroscience and Flight Mechanics Division at the Johnson Space Center. I would like to thank Dave Kanipe and Mark Hammerschmidt for providing me the opportunity to pursue this research, and especially my mentor Al Strahan for working with me on this project during the past year and a half.

I am grateful to my parents, my sister and my brother for their love and support during my time away from home. All of those encouragement phone calls from my four grandparents also made a difference. My aunt Vicky, who I called almost on a daily basis to try and translate into Spanish what life as a graduate student is like, has been a great friend to me.

My friends in the aerospace department have been amazing. My life would not have been the same without all the officemate story-telling, group studying, team debugging, and all of our “free time” spent together. The time I spent working on

this thesis would not have been the same without Stefanie. In addition to being my thesis-writing and code-debugging friend, she has been my running, and coffee shop friend for many months, and my homework and studying friend since the days when we were still trying to figure out what engineering was all about. Finally, I cannot express my gratitude to Daniel, Theresa, Lesley, and Elisa who took the time to read and edit this thesis, and Majji for his invaluable feedback.

TABLE OF CONTENTS

CHAPTER Page

LIST OF TABLES

LIST OF FIGURES

FIGURE Page

NOMENCLATURE

Variable	Definition	Units
c_D	Coefficient of Drag	
c_L	Coefficient of Lift	
c_{l_β}	Rolling Moment Stability Derivative	
c_{m_α}	Pitching Moment Stability Derivative	
c_{n_β}	Yawing Moment Stability Derivative	
D	Drag Vector	N
h	Altitude	km
L	Lift Vector	N
l_{ref}	Reference Length	m
S_{ref}	Reference Area	m^2
q	Classical Rodrigues Parameter Vector	
x_{cg}	Center of Gravity x Coordinate	m
y_{cg}	Center of Gravity y Coordinate	m
z_{cg}	Center of Gravity z Coordinate	m

Variable	Definition	Units
α	Angle-of-Attack	*deg*
β	Sideslip angle	deg
γ	Flight Path Angle	deg
Γ	Learning Rate	deg
ξ	Heading Angle	deg
ϕ	Bank Angle	deg
Φ	Roll Angle	deg
Ψ	Yaw Angle	deg
ω	Angular Velocity	deg/s

Acronym	Definition
CRP	Classical Rodrigues Parameters
EDL	Entry, Descent, and Landing
EI	Entry Interface
JSC	Johnson Space Center
MRAC	Model Reference Adaptive Control
NASA	National Aeronautics and Space Administration
RCS	Reaction Control System
SAMI	Structured Adaptive Model Inversion
SMRAC	Structured Model Reference Adaptive Control

CHAPTER I

INTRODUCTION

The new vision for space exploration will focus on sending humans to the moon and then to Mars. There are several challenges with manned Mars missions that did not exist in past robotic missions. One example is the need for precision landing so that a family of vehicles can be sent to the same location on the surface. Vehicles must land in close proximity to each other to provide the crew with easy access to all paylods. High landing accuracy will be required, and in order to achieve this level of accuracy a controlled entry trajectory is critical. In addition, crewed missions will require not only hundreds of pounds of equipment, consumables, and experiments, but also additional living space for the astronauts during the many months they will be traveling to Mars. As a result, a larger and heavier vehicle is needed. The Mars ellipsled [5] described in this thesis is one potential vehicle that meets these requirements.

One of the biggest challenges with the design of a guidance law or controller for a Mars vehicle is the uncertainty in the atmosphere characteristics. The Mars atmosphere has significant variations in density as well as strong and sudden wind gusts that change greatly with seasons and with latitude and longitude [6] [7]. In addition to the environmental uncertainties, the vehicle properties of a manned spacecraft are very likely to change during several months of travel. As a result, the controller must be able to compensate for any fluctuations in mass or vehicle properties such as the changes in the center of gravity (c.g.) of the spacecraft.

Significant research has been performed to develop guidance and control algo-

---

This thesis follows the style of *IEEE Transactions on Automatic Control.*

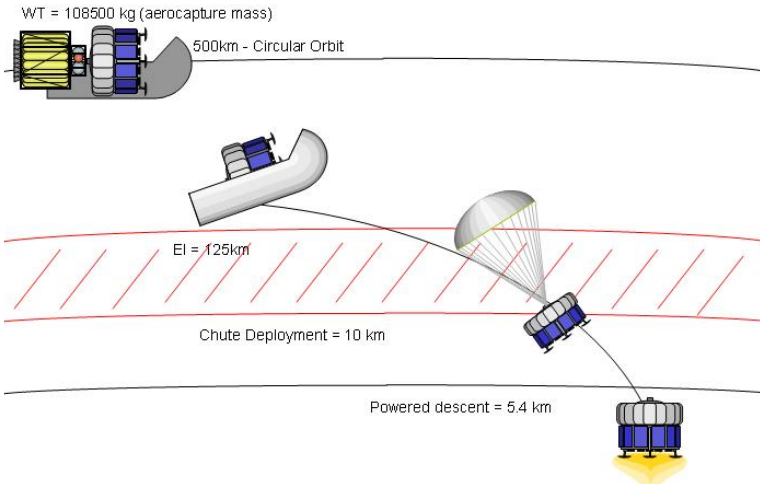

Fig. 1. Ellipsled Entry Trajectory [1]

rithms for Mars entry. For example, [8] and [9] use neural networks in the guidance laws to compensate for the large uncertainties in the Martian atmosphere. Reference [10] describes the entry, descent, and landing phases for the Mars Exploration Rover missions. The vehicles were uncontrolled until a radar altimeter sensed the ground and then a solution was calculated to fire the retro-rockets for the powered descent phase. Reference [11] describes the use of a proportional-integral-derivative controller to fire the retro-rockets during the powered descent phase.

The goal of this research is to develop an adaptive control system that can handle significant environment and vehicle model uncertainties from entry interface (EI) as labeled in Figure 1 until parachute deployment for the Mars ellipsled. Adaptive control is a viable solution to this problem because it is capable of calculating its own gain values while tracking a given reference trajectory. By having the gains adapt themselves with time, the uncertainties in the atmosphere and vehicle properties are taken into account, and the controller is able to follow the command.

Two different adaptive control algorithms will be evaluated. Initially, the conventional Model Reference Adaptive Control (MRAC) that has been previously de-

veloped by Annaswamy and Narendra [12] will be used. The second method will use the Structured Adaptive Model Inversion (SAMI) control algorithm developed at Texas A&M University [13].

This thesis is organized as follows. Initially, a brief description of the Mars entry problem is described in Chapter II. This includes a brief history of previous missions as well as an overview of current research. A description of the Mars ellipsled is presented in Chapter III. The development of the controllers is detailed in the subsequent chapters, and the implementation of both the system and control equations in the simulation used in this research is explained. Subsequently, the experiment design chapter describes steps to evaluate the controller performance. Finally, results, conclusions and recommendations are presented.

CHAPTER II

MARS ENTRY

The Mars entry problem is challenging in many different ways. The variability in atmospheric characteristics of the planet present challenges that do not exist when entering Earth or landing on the moon. One of the more significant challenges when entering another planet's atmosphere are the errors in position and velocity estimates from guidance at entry interface. Initial errors are difficult to correct and may result in missing the target later on. Therefore, the guidance system must be flexible enough to handle large initial errors.

The Martian atmosphere is dense enough to create significant heat rates and aerodynamic loads, which make it possible to skip out of the atmosphere. At the same time, it is not dense enough to slow the vehicle down as much as the Earth's atmosphere does. This has implications on the design of the trajectory since the vehicle must slow down in time for safe parachute deployment and landing. Typically, a single parachute is used to slow down the vehicle, but for a heavy vehicle such as the ellispled, the use of an additional supersonic parachute will be necessary. Another aspect to consider is the entry interface velocity of the vehicle; higher velocities will present more difficulties in the design of the entry trajectory.

Currently, the most accurate model of the martian atmosphere, the Mars-GRAM [2], is still not able to predict accurately the density and temperature variations or the strong and sudden wind gusts [14] [15]. These properties also vary largely with seasons and latitude. All these factors present major challenges when designing guidance and control systems for Mars vehicles.

Another challenge that arises during Mars entry is the lack of translational controls on the vehicle. The only controls on this type of vehicle are rotational, which

means the vehicle can maneuver solely by banking about the velocity vector following a series of roll reversals. Unlike the moon landing where retro-rockets were used to slow down the vehicle, a Mars lander can only use these during the terminal descent phase when the dynamic pressure is low enough.

As mentioned previously, the strict landing accuracy requirements are another challenge. Past Mars robotic missions such as the Mars Pathfinder and the Mars Exploration Rovers [10] [16] had landing ellipses of approximately 100 km and an uncontrolled ballistic entry was suitable. However, future manned missions will have landing requirements on the order of 5 km [17] [18]. Having an active guidance system onboard the vehicle will be critical to meet landing accuracy requirements.

Current research is being performed in order to meet strict landing requirements. Programs such as the Mars Science Laboratory and the Mars Surveyor are being used as prototype missions to design advanced guidance and control laws for Mars entry. Past knowledge with Earth controlled re-entry missions such as the Apollo and Mercury programs is being used as the basis for current Mars entry work by using Apollo-derived entry guidance algorithms [17] [18].

A typical Mars entry vehicle consists of several parts: a lander containing a payload, an aeroshell that protects the lander from heating and aerodynamic forces during the atmospheric entry phase, and a parachute that helps the vehicle slow down and separate from the aeroshell. A typical Mars entry trajectory has the following phases:

- Deorbit burn: The vehicle slows down from its orbital speed and reorients to its entry interface attitude before entering the atmosphere. It maneuvers to the trim angle-of-attack and the correct initial flight path angle.

- Atmospheric entry: The vehicle flies through the atmosphere and tracks a tra-

jectory. The trajectory is calculated in real time by the guidance system.

- Parachute phase: The vehicle is slowed down further with the parachute, and the lander is separated from its aeroshell.

- Terminal descent: The vehicle detaches from the parachute and lands in a controlled manner. Typically retro-rockets fire to further slow down and reorient the lander to avoid any terrain hazards on the surface of Mars.

A. Entry Guidance and Control

The entry problem is generally divided in two parts: guidance design, and control design. The guidance system calculates the entry trajectory in real time; the calculation is based upon heat load and aerodynamic load constraints. The control system then generates real-time attitude commands that will track the trajectory generated by the guidance system. In other words, the aerodynamic forces are modulated to ensure satisfactory tracking of the reference trajectory that is being generated by an active guidance system.

1. Guidance

Trajectory generation is an optimization problem. Typically, the final altitude is maximized. This allows additional flight time in the case where the optimal conditions for the deployment of the parachute have not yet been reached. The optimization problem has path constraints on heat loads, g-loads, and dynamic pressure. An active guidance routine calculates what the flight path angle, γ, should be in order to reach the final target.

Current research on guidance algorithms for Mars missions are derived from the Apollo command capsule guidance since this algorithm is already man-rated. This

algorithm seeks to minimize errors in inertial position with respect to the landing target. Additionally, direct control of the angle-of-attack is not available. The aeroshell generates lift with a c.g. offset and is designed to be trimmed during all phases of flight. To follow the trajectory generated by guidance, the magnitude of the lift and drag vectors are controlled by bank reversals. This is how the vehicle achieves the desired drag acceleration profile to meet its target. Guidance equations typically assume that the vehicle flies at its trim condition, and is modeled as a point mass for the purpose of generating a trajectory. The only out-of-plane effect comes from the bank angle ϕ which changes the lift component perpendicular to the velocity vector from L to $L\cos\phi$, and makes the vehicle descend at a steeper or shallower flight path angle.

The Mars Exploration Rovers (MER) are another example of vehicles with passive entry capsules. The aeroshell for this vehicle completely relies on aerodynamic stability to perform a controlled entry during all phases of flight including the parachute phase. This design has good stability properties that minimize the angle-of-attack excursion [10]. Other vehicles that have similar guidance systems are the Mars Science Laboratory mission [9] and the HL-20 [19], which is an Earth entry vehicle.

2. Control

Ballistic entry vehicles have typically been designed with phase plane controllers that simply roll the vehicle to the commanded bank angle. Most of the work is done by the guidance system, and the controller only needs to provide the necessary bank angle. Most entry vehicles use reaction control system (RCS) jets as their only control effectors. Vehicles such as the Space Shuttle orbiter, NASA's X-38, or HL-20 that are designed to enter Earth's atmosphere have aerodynamic control surfaces in addition to RCS jets. However, Mars entry vehicles would not benefit the same way from

having aerodynamic control surfaces while flying through a low density atmosphere. As a result, Mars vehicles have rotational controls only. The controls are used to roll the vehicle about the velocity vector through several bank reversals commanded by guidance. By changing the bank angle, the magnitudes of the lift and drag vectors are modulated in order to obtain the necessary lift-to-drag ratio to reach a target.

B. The Mars Atmosphere

The observational data available for the Mars atmosphere is very sparse compared to the data for the Earth's atmosphere. Models such as the Mars-GRAM (Global Reference Atmosphere Model) [2] and [20] are based on interpolation between the available observations and are subject to high uncertainties. Several researchers have attempted to model the Martian atmosphere. However, since the data available is limited, they have focused on representing the variability of the atmospheric properties. For example, Justus et al. [2] compare the Mars Global Surveyor with the Mars-GRAM atmospheric model to show that the model is accurate, yet density variations are still a concern for Mars mission designers. Figure 2 is a good representation of how the density for a given altitude can vary greatly with solar longitude, L_s. Another example of density variations in the Mars atmosphere is presented in reference [3]. The Mars-GRAM model was used for the design of the Mars Pathfinder mission, and density variations were taken into account. Figure 3 is a graphic representation of the density variations for different atmospheric models. In addition to atmospheric parameter variations, winds are an important issue to consider when designing a guidance system. For example, the recent Mars exploration Rover missions used [11] for wind variations during entry at both sites. This research uses the Mars-GRAM in the simulations, and as a basis to compare the results for cases with atmospheric density

uncertainties.

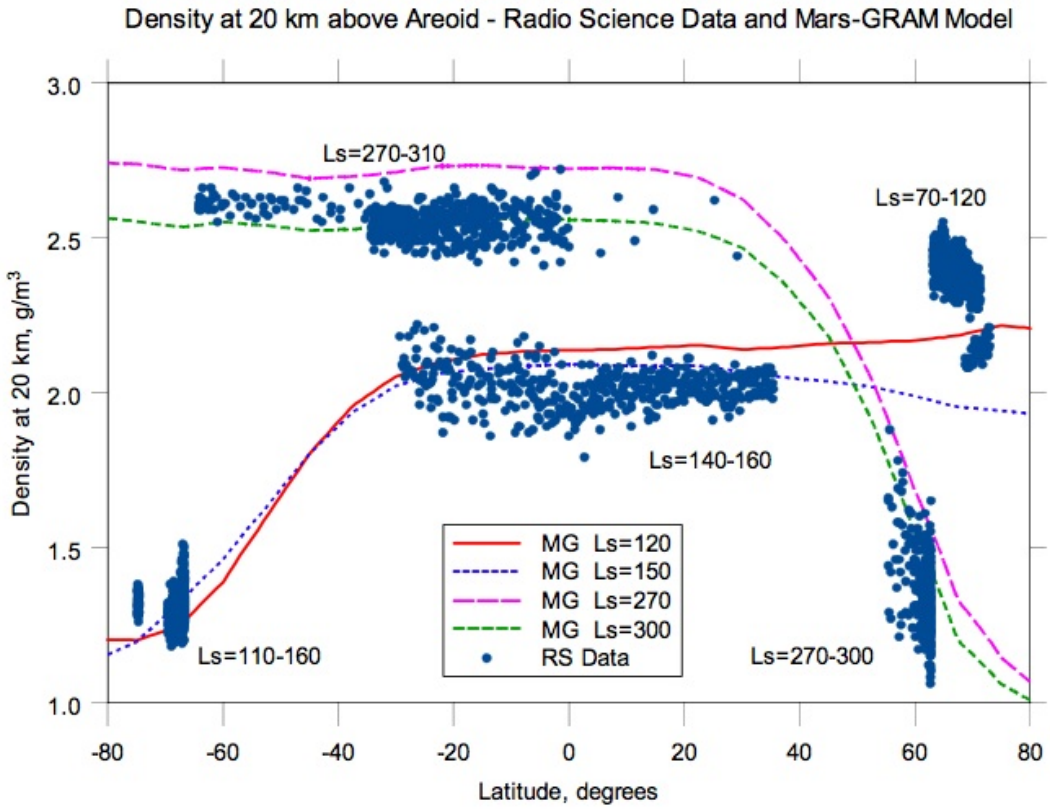

Fig. 2. Comparison of Density at 20 km Altitude from Mars Global Surveyor Radio Science Observations and Mars-GRAM 2001 [2]

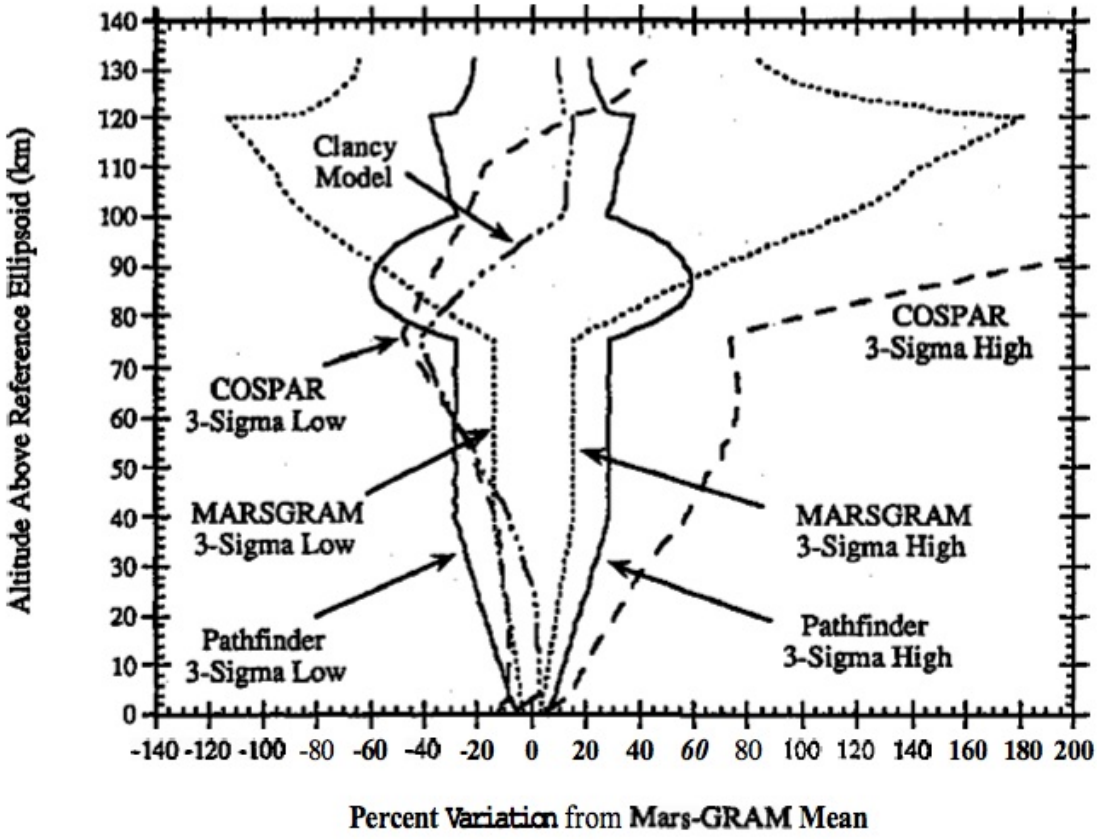

Fig. 3. Mars Atmospheric Density Models Compared to Mars-GRAM Mean [3]

CHAPTER III

THE MARS ELLIPSLED

Future manned missions to Mars will require much larger vehicles than those used in the past. The missions will last several months, and vehicles must be able to provide life support for the crew, as well as carry large quantities of consumables and scientific equipment. Manned spacecraft for Mars will be large and heavy. The conical shapes used previously for robotic missions or relatively short lunar manned missions will not suffice. If we were to scale up the same conical shape, the resulting vehicle would be so large in diameter that it might not fit on a rocket. The ellispled is an alternate shape for an aeroshell that could carry several metric tons stacked along the length of the vehicle and still fit in an existing launch vehicle. This chapter describes in detail both the Mars ellipsled and a sample mission to Mars.

The ellipsled can carry up to six crew members to Mars. It weighs up to 78 metric tons and has a length of approximately 20 meters (Figure 4). One of the main advantages of using an aeroshell with this shape is that it was designed to be one half of the launch shroud on Earth, which means we can bring this weight up with no extra cost. Another advantage of this shape is the increase in lift-to-drag to approximately 0.46. This value has typically been around 0.3 for conical shapes like the Apollo entry capsules. A previous study performed at the Johnson Space Center [1] concluded that the ellipsled has enough stability and flight mechanics margins to take humans to Mars [5].

A scaled down model of the ellipsled was used for this research. The vehicle was modeled as a cylinder with a diameter of 3.75 meters, a length of 6.323 meters, and a mass of 3000 kilograms. The center of gravity in the x direction, x_{cg}, and in the z direction, z_{cg}, are offset for maneuverability. Tables I and II list the mass

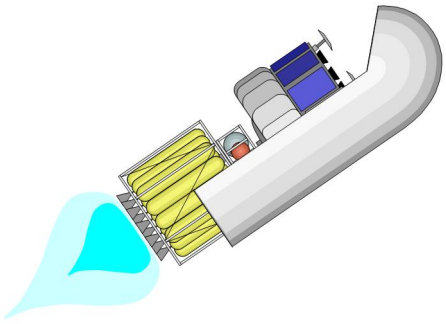

Fig. 4. Mars Ellipsled [1]

and geometric properties of the ellipsled. The ellipsled has eighteen reaction control system jets located in the aft part of the vehicle. There are nine jets on each side: three side jets, three up jets, and three down jets. The three side jets are used for yaw control, and the up and down jets are used for pitch and roll control. The yaw jets can produce a torque up to ninety-five Newtons each and the pitch and roll jets produce a torque of fourteen Newtons each. Table III provides information about the location and thrust for each of the jets. The RCS jets are designed to provide at least five degrees per second of angular rates. They are used to keep the angle-of-attack at its trim value and to roll the vehicle about the velocity vector to track a bank angle profile. For this research, it is assumed that the moment arms of the RCS jets are constant with respect to the center of gravity of the vehicle. Additionally, it is assumed that there is no change in mass or inertia properties due to fuel consumption. The aerodynamic data used here was obtained from [1] and it is presented in Table IV.

An example mission would take two ellipsleds to Mars. One would carry an astronaut habitat and the other one would carry the crew and life support equipment. Both vehicles need to land at approximately the same location on the Mars surface.

Table I. Ellipsled Mass and Inertia Properties

mass	3000 kg
I_{xx}	2983 $kg \cdot m^2$
I_{yy}	4909 $kg \cdot m^2$
I_{zz}	5683 $kg \cdot m^2$

Table II. Ellipsled Geometric Properties

Reference area	S	11.045 m^2
Reference Length	l	6.323 m
x center of gravity	x_{cg}	0.182 m
y center of gravity	y_{cg}	0 m
z center of gravity	z_{cg}	-0.175 m

Table III. Reaction Control System Jets

	Moment ($N \cdot m$)	Moment arm (m)	Thrust (N)
roll (2 jets)	105	1.88	28
pitch (2 jets)	166	2.98	28
yaw (1 jet)	284	2.98	95

Table IV. Ellipsled Aerodynamics

α	C_L	C_D	C_{n_β}	$C_{m\alpha}$	C_{l_β}
45^o	0.652	1.568	-0.02	0.037	-2.279
50^o	0.659	1.740	0	0.019	-2.354
55^o	0.633	1.910	.015	0.000	-2.414
60^o	0.573	2.069	.034	-0.211	-2.462
65^o	0.481	2.208	.05	-0.428	-2.495

CHAPTER IV

MARS ENTRY SIMULATION

This chapter outlines the entry simulation used to evaluate the performance of the two adaptive control systems mentioned previously. It includes a detailed development of the translational and rotational equations of motion for the ellipsled. The simulation is nonlinear and its five degrees-of-freedom include the altitude above the surface of the planet, the downrange distance, and the three rotational degrees of freedom.

A scaled down version of the ellipsled was used in the simulation. The mass and inertia properties, and aerodynamics of the ellipsled are shown in Tables I, II, and IV respectively. The ellipsled is modeled as a rigid cylinder with a symmetric inertia matrix. Reference [1] concluded that the trim angle-of-attack for the ellipsled is 55 degrees, and the center of gravity of the cylinder is shifted in the x and z direction by the following amounts:

$$x_{cg} = 0.182\ m \tag{4.1}$$

$$z_{cg} = -0.175\ m \tag{4.2}$$

A three degree-of-freedom nonlinear open-loop simulation was performed to show the trim angle-of-attack, α, of the ellipsled. Figure 5 shows the pitching motion of the cylinder for thirty seconds given three different initial values for α. Clearly, when given an initial value of $\alpha = 55^o$, the vehicle remains well trimmed. The ellipsled is stable in pitch, therefore, it will be assumed that the angle-of-attack is constant throughout the simulation.

As mentioned in previous chapters, the entry problem is typically divided into two parts: guidance or trajectory generation and control design. The translational equations of motion are part of the guidance system, and the rotational equations of

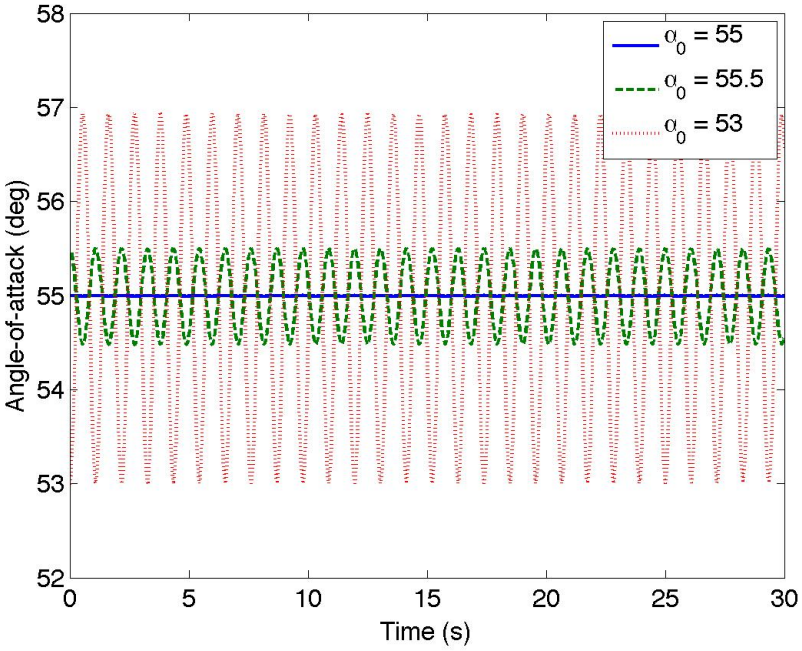

Fig. 5. Ellipsled Trim Angle-of-Attack

motion are part of the control system. The following section develops both translational and rotational equations for the ellipsled during its entry phase.

A. Translational Equations of Motion

The translational kinematics for the mass center of the vehicle are given in an inertial, planet-fixed frame as shown in Figure 6. This figure shows the velocity vector at the mass center which is related to the inertial reference frame $\{\mathbf{i}\}$ through two angles: the heading angle ξ, and the flight path angle γ. The velocity vector $\mathbf{v}$ can be expressed in cartesian coordinates:

$$\mathbf{v} = \dot{x}\hat{\mathbf{i}}_\mathbf{1} + \dot{y}\hat{\mathbf{i}}_\mathbf{2} + \dot{z}\hat{\mathbf{i}}_\mathbf{3} \tag{4.3}$$

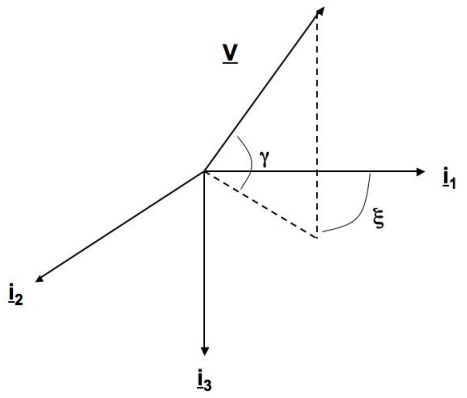

Fig. 6. Inertial Reference Frame

where $\dot{z} = -\dot{h}$, and h is the altitude. This vector can also be expressed in a different set of coordinates as a function of its magnitude $v = |\mathbf{v}|$ and the angles ξ and γ:

$$\mathbf{v} = v\cos\gamma\cos\xi\ \hat{\mathbf{i}}_\mathbf{1} + v\cos\gamma\sin\xi\ \hat{\mathbf{i}}_\mathbf{2} - v\sin\gamma\ \hat{\mathbf{i}}_\mathbf{3} \tag{4.4}$$

By setting both equations equal to each other, it is possible to obtain equations for one set of coordinates in terms of the other set of coordinates as follows:

$$\dot{x} = v\cos\gamma\cos\xi \tag{4.5}$$

$$\dot{y} = v\cos\gamma\sin\xi \tag{4.6}$$

$$\dot{h} = -v\sin\gamma \tag{4.7}$$

where x is the downrange distance, y is the crossrange distance, and h is the altitude above the surface of Mars. For this research, the heading angle is assumed to be zero due to the lack of an active guidance scheme.

The above translational equations of motion are written in the inertial frame. However, it is also necessary to write them in a body-fixed frame with the origin at the mass center of the vehicle. The direction cosine matrix to transfer from the

inertial frame $\{\mathbf{i}\}$ to the body-fixed frame $\{\mathbf{b}\}$ is calculated using a 3-2-1 Euler angle sequence through the yaw angle Ψ, the pitch angle Θ, and the roll angle Φ. The rotation matrix is given by

$$[\mathbf{n}]_b = [C_1(\Phi)]\ [C_2(\Theta)]\ [C_3(\Psi)]\ [\mathbf{n}]_i \tag{4.8}$$

The translational equations for the center of mass can now be written in the body frame as a function of the magnitude of the velocity vector and the aerodynamic angles α and β as shown in equation 4.9. Figure 7 is a graphic representation of this.

$$[\mathbf{v}]_b = \begin{bmatrix} v\cos\beta\cos\alpha \\ v\sin\beta \\ v\cos\beta\sin\alpha \end{bmatrix} \tag{4.9}$$

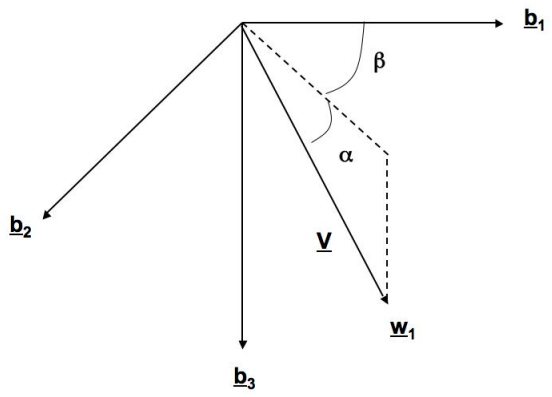

Fig. 7. Body-Fixed Reference Frame

The translational kinematics have been developed in the body frame; now, the dynamics will be derived. The external forces acting on a ballistic entry vehicle are the aerodynamic forces and the gravity force. These forces are typically expressed in a reference frame called the wind frame $\{\mathbf{w}\}$. In order to obtain the forces for the translational equations for the vehicle coordinatized in the wind frame, it is necessary

to describe the relationship between the body frame, inertial frame, and the wind frame. To transfer from the inertial frame to the wind frame another 3-2-1 Euler angle sequence is used. In this transformation, the frame is rotated through the heading angle, ξ, the flight path angle, γ, and bank angle, ϕ. A graphic representation of this is given in Figure 8.

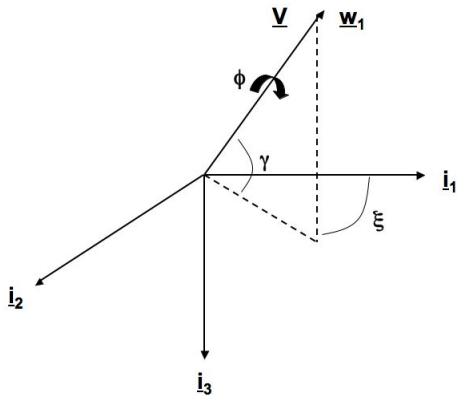

Fig. 8. Wind Reference Frame

In general, the coordinatization of any vector in the wind frame is given by:

$$[\mathbf{n}]_w = [C_1(\phi)]\ [C_2(\gamma)]\ [C_3(\xi)]\ [\mathbf{n}]_i \tag{4.10}$$

Now the dynamic equations for the vehicle can be written in the wind frame. Consider the special case where the heading angle $\xi = 0$. First, the kinematics for the mass center will be developed, and subsequently the forces acting on the vehicle will be described with a free body diagram. The translational kinematics for the center of mass are given by:

$$\mathbf{v} = v\ \hat{\mathbf{w}}_\mathbf{1} \tag{4.11}$$

$$\mathbf{a} = \frac{^w d}{dt}(\mathbf{v}) + \omega_{w/i} \times \mathbf{v} \tag{4.12}$$

where

$$[\omega_{w/i}]_w = \begin{bmatrix} -\dot{\xi}\sin\gamma + \dot{\phi} \\ \dot{\xi}\cos\gamma\sin\phi + \dot{\gamma}\cos\phi \\ \dot{\xi}\cos\gamma\cos\phi + \dot{\gamma}\sin\phi \end{bmatrix} \tag{4.13}$$

Substituting $[\omega_{w/i}]_w$ into the acceleration equation, the following is obtained.

$$\mathbf{a} = \dot{v}\hat{\mathbf{w}}_\mathbf{1} - v\dot{\gamma}\sin\phi\hat{\mathbf{w}}_\mathbf{2} - v\dot{\gamma}\cos\phi\hat{\mathbf{w}}_\mathbf{3} \tag{4.14}$$

There are three external forces acting on the ellipsled as shown in Figure 9: lift, drag, and gravity. The lift vector, **L**, is perpendicular to the velocity vector, and the drag vector, **D**, is in the opposite direction of the velocity vector. The gravity vector, **g**, points in the positive z-axis of the planet-fixed reference frame. The forces in Newtons are calculated in equations 4.15 - 4.17.

$$\mathbf{L} = -\bar{q}Sc_{L_\alpha}\alpha\hat{\mathbf{w}}_\mathbf{3} \tag{4.15}$$

$$\mathbf{D} = -\bar{q}Sc_{D_\alpha}\alpha\hat{\mathbf{w}}_\mathbf{1} \tag{4.16}$$

$$\mathbf{g} = mg\hat{\mathbf{w}}_\mathbf{3} \tag{4.17}$$

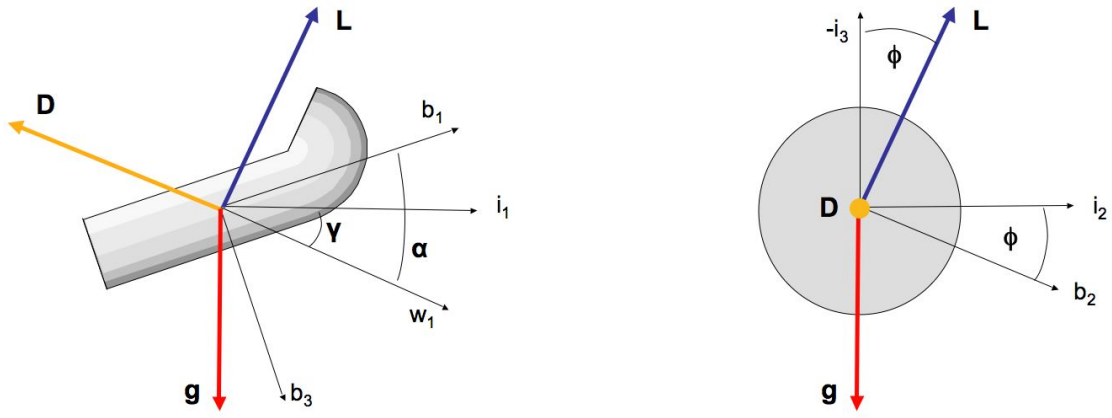

(a) Side view (b)Back view

Fig. 9. Ellipsled Free Body Diagram

The total force vector, $\mathbf{F}$, can now be written as follows.

$$[\mathbf{F}]_w = \begin{bmatrix} -D - mg\sin\gamma \\ mg\cos\gamma\sin\phi \\ -L + mg\cos\gamma\cos\phi \end{bmatrix} \tag{4.18}$$

From Newton's second law, the dynamic translational equations of the mass center of the vehicle are given by

$$[\mathbf{F}]_w = m\ [\mathbf{a}]_w \tag{4.19}$$

$$-D - m\ g\sin\gamma = m\dot{v} \tag{4.20}$$

$$mg\cos\gamma\sin\phi = -mv\dot{\gamma}\sin\phi \tag{4.21}$$

$$-L + mg\cos\gamma\cos\phi = -mv\dot{\gamma}\cos\phi \tag{4.22}$$

Rearranging the first equation, and adding the second and third equations, the equations become:

$$\dot{v} = -\frac{D}{m} - g\sin\gamma \tag{4.23}$$

$$\dot{\gamma} = \frac{L}{mv}\cos\phi - \frac{g}{v}\cos\gamma \tag{4.24}$$

These equations are the translational equations of motion or guidance equations for the ellipsled.

B. Rotational Equations of Motion

This section outlines the development of the rotational equations of motion for the vehicle about its mass center. The rotational kinematic equations for the ellipsled

can be expressed in the body frame:

$$\begin{bmatrix} \dot{\Psi} \\ \dot{\Theta} \\ \dot{\Phi} \end{bmatrix} = [A_{321}(\Psi\ \Theta\ \Phi)]\ [\omega]_b \tag{4.25}$$

Here, A_{321} is the direction cosine matrix to go from the inertial frame to the body frame. The angular velocity of the vehicle in the body-fixed frame can also be written as follows:

$$[\mathbf{w}_{b/i}]_b = [\mathbf{w}_{b/w}]_b + [\mathbf{w}_{w/i}]_b \tag{4.26}$$

or using the direction cosine matrix to go from the wind frame to the body frame,

$$[\mathbf{w}_{b/i}]_b = [C_w^b]([\mathbf{w}_{b/w}]_w + [\mathbf{w}_{w/i}]_w) \tag{4.27}$$

The matrix $[C_w^b]$ is given in terms of the aerodynamic angles α and β from Figure 7,

$$[C_w^b] = [C_2(\alpha)]\ [C_3(-\beta)] = \begin{bmatrix} \cos\alpha\cos\beta & -\cos\alpha\sin\beta & -\sin\alpha \\ \sin\beta & \cos\beta & 0 \\ \sin\alpha\cos\beta & -\sin\alpha\sin\beta & \cos\alpha \end{bmatrix} \tag{4.28}$$

and the body angular velocity is

$$\omega_{b/w} = \dot{\alpha}\hat{\mathbf{b}}_\mathbf{2} - \dot{\beta}\hat{\mathbf{w}}_\mathbf{3} \tag{4.29}$$

However, it was assumed earlier that the angle-of-attack, α, is held constant throughout the simulation; thus, the angular velocity coordinatized in the wind frame can be written as follows:

$$[\omega_{b/w}]_w = [\ 0 \quad 0 \quad -\dot{\beta}\ ]^T \tag{4.30}$$

Substituting equations 4.30, 4.28, and 4.14 into equation 4.26, the rotational kinematic equations for the ellipsled are obtained.

$$\begin{bmatrix} p \\ q \\ r \end{bmatrix} = \begin{bmatrix} \cos\alpha\cos\beta & -\cos\alpha\sin\beta & -\sin\alpha \\ \sin\beta & \cos\beta & 0 \\ \sin\alpha\cos\beta & -\sin\alpha\sin\beta & \cos\alpha \end{bmatrix} \begin{bmatrix} \dot{\phi} \\ \dot{\gamma}\cos\phi \\ -\dot{\beta} - \dot{\gamma}\sin\phi \end{bmatrix} \tag{4.31}$$

Rearranging,

$$\begin{bmatrix} p \\ q \\ r \end{bmatrix} = \begin{bmatrix} \cos\alpha\cos\beta & -\cos\alpha\sin\beta\cos\phi + \sin\alpha\sin\phi & \sin\alpha \\ \sin\beta & \cos\beta\cos\phi & 0 \\ \sin\alpha\cos\beta & -\sin\alpha\sin\beta\sin\phi - \cos\alpha\sin\phi & -\cos\alpha \end{bmatrix} \begin{bmatrix} \dot{\phi} \\ \dot{\gamma} \\ \dot{\beta} \end{bmatrix} \tag{4.32}$$

Taking the inverse of equation 4.32 we have:

$$\begin{bmatrix} \dot{\phi} \\ \dot{\gamma} \\ \dot{\beta} \end{bmatrix} = \begin{bmatrix} \cos\alpha\cos\beta & \sin\beta & \sin\alpha\cos\beta \\ -\sin\alpha\cos\beta/\cos\phi & \cos\beta/\cos\phi & -\sin\alpha\sin\beta/\cos\phi \\ \cos\alpha\sin\beta\tan\phi + \sin\alpha & -\cos\beta\tan\phi & \sin\alpha\sin\beta\tan\phi - \cos\alpha \end{bmatrix} \begin{bmatrix} p \\ q \\ r \end{bmatrix} \tag{4.33}$$

Equation 4.33 is the kinematic equation for the ellispled. This matrix is not a conventional kinematic matrix. This is due to the fact that the reference trajectory is given in the wind frame. To determine if this matrix is singular at any given time, its determinant was calculated and set equal to zero. The determinant is a function of the angle-of-attack, the sideslip angle, the bank angle, and the flight path angle. Since the ellipsled is always at its trim angle-of-attack, the matrix does not become singular.

The ellipsled is assumed to be a rigid body, so Euler's rotational equations are used.

$$[I]\dot{\omega} + \omega \times [I]\omega = \mathbf{f} \tag{4.34}$$

Here, $\mathbf{f}$ is the sum of the aerodynamic moments L, M, and N, and the control input $\mathbf{u}$ from the reaction control system jets. The magnitudes of the aerodynamic moments are the following.

$$L = \bar{q}\ S_{ref}\ l_{ref}\ c_{l_\beta}\beta \tag{4.35}$$

$$M = \bar{q}\ S_{ref}\ l_{ref}\ c_{m_\alpha}\alpha \tag{4.36}$$

$$N = \bar{q}\ S_{ref}\ l_{ref}\ c_{n_\beta}\beta \tag{4.37}$$

The magnitude of the control input, $\mathbf{u}$, is given by thrust times the moment arm for each jet. The controller design is described in detail in the following chapter.

There are several papers in the literature that discuss optimal guidance and use similar point mass translational equations plus the bank angle equation to calculate the necessary entry trajectory in terms of bank angle commands. Some examples of problems that use these equations can be found in [19] [18] [8]. In these examples, as well as for the ellipsled, the only two states that are controlled are the angle-of-attack which is regulated to its trim value, and the bank angle to track the necessary roll reversals commanded by guidance.

CHAPTER V

ADAPTIVE CONTROL

Designing a controller for a physical system presents several challenges. Typically, the balance between model fidelity and simplicity of the mathematical model of a system is difficult to achieve. In addition, there are always a number of unexpected errors or variations in the model of a system and of the environment in which it operates. The main goal of a control system is to maintain the system operating correctly despite all modeling errors and sudden changes in its operating conditions.

For systems that have known bounds on the uncertainties, it is possible to design a controller that can be tuned ahead of time to compensate for these errors. Gain scheduling [21] and robust control [22] are two such methods for this. The Space Shuttle is one example of a vehicle that uses gain scheduling during entry [23]. The scheduling is based on dynamic pressure and Mach number. However, these methodologies work on Earth because it is possible to obtain highly accurate atmospheric data. In cases where the system uncertainties are large and highly unpredictable, such as the atmospheric density and wind gusts in the Martian atmosphere, it is impractical and inefficient to use these methodologies. Systems that operate in a highly uncertain environment or that contain uncertainties in the plant parameters require a continuous adaptation of the control system to be able to achieve acceptable performance levels.

Adaptive control [12] [21] [24] [4] is a particularly suitable scheme for systems that have uncertain parameters before and during their operation. An adaptive controller can tune its own gains in real time through a learning mechanism based on current performance.

There are two types of adaptive control. The first one is called Model-Reference

Adaptive Control (MRAC) and the second one is called Self-tuning Control [4]. The main difference between these two methods is that a MRAC controller directly calculates the control law based on measured signals whereas a self-tuning controller estimates the plant parameters based on the reference plant parameters and calculates the control law indirectly based on these estimates. For this research, two controllers are designed and implemented. The first controller is based on the standard MRAC model found in the literature [12] [21] [24] [4], and the second controller is based on a design developed at Texas A&M University called Structured Adaptive Model Inversion Control (SAMI). The following two sections describe both MRAC and SAMI in more detail. The most important difference between the two designs is that the MRAC controller adapts the controller gains in order to achieve tracking error convergence, and the SAMI controller can adapt specifically for the lack of knowledge in the vehicle properties or Mars atmospheric properites.

A. Model-Reference Adaptive Control

The goal of a MRAC system is to track the output of a reference model by enforcing error convergence. This is done by continuously calculating the controller gains through an adaptation mechanism. A block diagram of a typical MRAC system [4] is presented in Figure 10.

The reference model is used to generate an ideal output, y_m, to be followed by the plant. However, it is not always necessary to have an ideal model to generate a reference trajectory. It is also possible to use a precomputed trajectory, which must meet certain conditions. For example, in the case of the Mars ellipsled, the reference trajectory would come from an active guidance routine. For the MRAC problem, the plant model contains several uncertain parameters but it has a known structure.

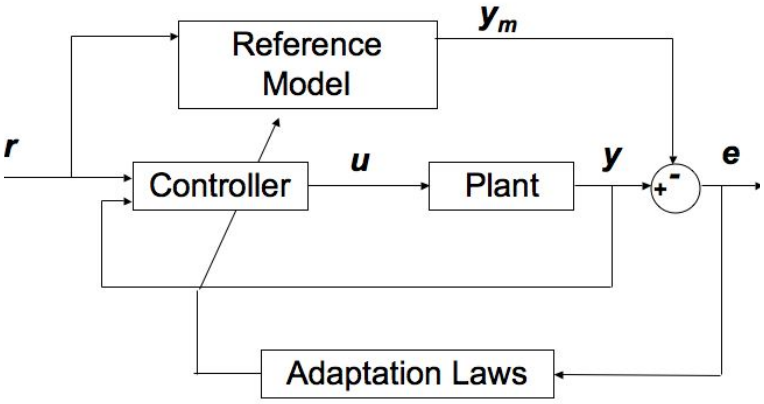

Fig. 10. MRAC Block Diagram [4]

The differential equation for the system or the reference model can be either linear or nonlinear. In general, it has the form of equation 5.1.

$$\dot{\mathbf{x}} \;=\; f(\mathbf{x}) + \mathbf{u} \tag{5.1}$$

The controller takes the error dynamics as an input to adjust its own gains with time. The error is the difference between the current output of the system and the reference trajectory. The control objective is to minimize the error between the outputs, and thus perfect tracking of the states is not always achieved. The adaptation mechanism for the control law can vary from one case to another depending on the form of the dynamic equations of the system. In general, it is possible to find a differential equation for each of the gains in the control law. These gains will learn with time what their ideal value should be in order to achieve convergence of the error. The control law u has the form of equation 5.2,

$$u = \widetilde{a}_r \omega_r + \widetilde{a}_\omega \omega \tag{5.2}$$

where ω and ω_r are the angular velocity and the reference angular velocity respectively, and $\widetilde{a}_r$ and $\widetilde{a}_w$ are the adaptive gains that change with time. Lyapunov stability

theory [4] [12] [21] is used to obtain the differential equations for these gains to ensure stable error dynamics. In this case, the Lyapunov function from equation 5.3, and its derivative shown in equation 5.4 are used to derive the adaptation equations for $\widetilde{a}_r$ and $\widetilde{a}_\omega$.

$$V(e, \widetilde{a}_r, \widetilde{a}_\omega) = \frac{1}{2}e^2 + \frac{1}{2\Gamma}|b_p|(\widetilde{a}_r^2 + \widetilde{a}_w^2) \tag{5.3}$$

$$\dot{V}(e, \dot{e}, \widetilde{a}_r, \dot{\widetilde{a}}_r, \widetilde{a}_\omega, \dot{\widetilde{a}}_\omega) = e\dot{e} + \frac{1}{\Gamma}|b_p|(\widetilde{a}_r\dot{\widetilde{a}}_r + \widetilde{a}_\omega\dot{\widetilde{a}}_\omega) \tag{5.4}$$

where $e = \omega - \omega_r$, and the subscript r denotes the reference. The error dynamics are substituted into the derivative of the Lyapunov function as follows:

$$\dot{e} = \dot{\omega} - \dot{\omega}_r \tag{5.5}$$

where

$$\dot{\omega} = f(\omega, I) + b_p u \tag{5.6}$$

$$\dot{\omega}_r = a_m\omega_r + b_m r \tag{5.7}$$

Combining the equations above, equation 5.8 is obtained.

$$\begin{aligned} \dot{e} &= f(\omega, I) + b_p u + a_m\omega_r - b_m r \\ &= f(\omega, I) + b_p(\hat{a}_r\omega_r + \hat{a}_\omega\omega) + a_m\omega_r - b_m r \end{aligned} \tag{5.8}$$

where $\hat{a}_r$ and $\hat{a}_\omega$ are the parameter estimates. Setting the derivative of the error (5.8) equal to zero and equating coefficients, the ideal values of the gains a_ω^* and a_r^* can be found.

$$f(\omega, I) + b_p(\hat{a}_r\omega_{ref} + \hat{a}_w\omega) = -a_m\omega_r - b_m r \tag{5.9}$$

$$a_\omega^* = -\frac{a_m}{b_p} - \frac{f(\omega, I)}{b_p\omega} \tag{5.10}$$

$$a_r^* = \frac{b_m}{b_p} \tag{5.11}$$

Clearly, the ideal values cannot be calculated since the true values for the plant parameters are unknown. This can be overcome by deriving adaptive laws for the error between the estimates and the true values instead of adaptive laws for the estimates directly. The following equations show the derivative of the error in terms of the true parameters and their estimates. These results will be substituted into the Lyapunov function in subsequent steps to finally obtain the adaptation laws for the controller gains.

$$\begin{aligned}
\dot{e} &= -a_m(\omega - \omega_r) + (a_m + b_p\hat{a}_\omega)\omega + f(\omega, I) + b_p(-b_m + \hat{a}_r b_p)r \\
&= -a_m e + (a_m + b_p\hat{a}_\omega)\omega + f(\omega, I) + b_p(-\frac{b_m}{b_p} + \hat{a}_r)r \\
&= -a_m e + (\frac{b_p a_m}{b_p} + b_p\hat{a}_\omega + \frac{f(\omega, I)b_p}{\omega b_p})\omega + b_p(-\frac{b_m}{b_p} + \hat{a}_r)r \\
&= -a_m e + b_p(\frac{a_m}{b_p} + \frac{f(\omega, I)}{\omega b_p} + \hat{a}_\omega)\omega + b_p(\hat{a}_r - a_r^*)r \\
&= -a_m e + b_p(\hat{a}_\omega - a_\omega^*)\omega + b_p(\hat{a}_r - a_r^*)r
\end{aligned} \tag{5.12}$$

where $\hat{a}_\omega$ and $\hat{a}_r$ are the estimated gains and a_ω^* and a_r^* are the ideal values of the gains. As mentioned earlier, it is desired to derive adaptive laws for the difference of the true parameters and their estimates. These new parameters are defined as follows:

$$\widetilde{a}_\omega = \hat{a}_\omega - a_\omega^* \tag{5.13}$$

$$\widetilde{a}_r = \hat{a}_r - a_r^* \tag{5.14}$$

The equation that describes the error dynamics becomes:

$$\dot{e} = -a_m e + b_p(\widetilde{a}_\omega\omega + \widetilde{a}_r r) \tag{5.15}$$

Substituting equation 5.15 into the expression for $\dot{V}$ in equation 5.4, the following is obtained.

$$\dot{V} = -a_m e^2 + b_p[(e\omega + \frac{1}{\gamma}\dot{\widetilde{a}}_w)\widetilde{a}_w + (er + \frac{1}{\gamma}\dot{\widetilde{a}}_r)\widetilde{a}_r] \tag{5.16}$$

Now the adaptive laws can be found. To ensure error convergence, the derivative of the Lyapunov function must always be a negative semidefinite function. This can be accomplished by setting the second and third terms of $\dot{V}$ equal to zero. The resulting equations dictate the adaptation mechanism for $\widetilde{a}_r$ and $\widetilde{a}_w$. These gains are proportional to a constant parameter Γ called the learning rate, which determines how fast the adaptation occurs as shown in equations 5.17 and 5.18.

$$\dot{\widetilde{a}}_r = -\Gamma e \omega_{ref} \tag{5.17}$$

$$\dot{\widetilde{a}}_w = -\Gamma e \omega \tag{5.18}$$

The selection of the learning rate, Γ, and initial values for the gains are tuning parameters for the controller which will be discussed later.

B. Structured Adaptive Model Inversion Control

The second adaptive control approach that will be used in this research is called Structured Adaptive Model Inversion (SAMI) control [25] [26]. This method is based on the concepts of structured model reference adaptive control (SMRAC) [13] as well as feedback linearization and dynamic inversion [4] [12] [21]. For dynamic inversion to work properly, it is necessary to have an accurate mathematical model of the plant so the dynamics can be cancelled out exactly. Since this is not possible due to the inherent uncertainties in physical systems, an adaptive controller is wrapped around the dynamic inversion controller to compensate for these errors.

Physical systems can generally be represented by second order differential equa-

tions or two sets of first order differential equations. The concept of SMRAC takes advantage of the fact that the equations of motion of a system can be separated into dynamic and kinematic parts. The kinematic equations are exactly known, and all of the uncertainties are in the dynamic equations [13]. Therefore, the adaptation mechanism for the system is only related to the momentum-level equations which contain the uncertain parameters such as mass and inertia.

Previously at Texas A&M University, SAMI has been applied to trajectory tracking with smooth maneuvers. The method can handle large model errors [27] and bounded disturbances. Specifically, it has been used for tracking of aggressive aircraft maneuvers [28] and spacecraft maneuvers with control moment gyros [29]. However, SAMI has certain limitations. It must track a singularity-free trajectory, and there can be no unmodeled dynamics. One of the challenges of this research is to use a SAMI controller to track a series of step commands. There is a singularity each time a new command is given. A smooth polynomial curve is fitted to the reference so the controller is able to track it. Regardless of whether the trajectory is smooth, there are still very steep curves which the SAMI controller must follow. This can require large control inputs.

The development of the SAMI equations for this thesis is based on the work of Subbarao [28]. The dynamic and kinematic equations have the form of equations 5.19 and 5.20:

$$\dot{q} = f(q, \omega) \tag{5.19}$$

$$\dot{\omega} = g(q, \omega, p) + h(q, \omega, p)u + H(q, \omega) \tag{5.20}$$

where q is the attitude vector expressed in terms of the Classical Rodrigues Parameters (CRP) [30] and ω is the angular velocity vector. The terms $f(q, \omega, p)$, $g(q, \omega, p)$,

$h(q, \omega, p)$, and $H(q, \omega, p)$ are continuous functions and p is a vector of uncertain parameters. For the Mars ellipsled, equation 5.19 is the kinematic equation for rigid body motion and equation 5.20 can be represented by Euler's rotational equations of motion as shown below.

$$\dot{q} = A(q)\ \omega \tag{5.21}$$

$$I\dot{\omega} = -\omega \times I\omega + u \tag{5.22}$$

Here, $A(q)$ is the kinematic matrix in terms of CRPs and u is the control input. Since the objective of the controller is to drive the tracking error to zero, the error dynamics are prescribed as follows:

$$\ddot{e} + C\dot{e} + Ke = 0 \tag{5.23}$$

where C and K are positive definite matrices chosen by the designer, and the error is defined as $e = q - q_r$. To obtain the first and second derivatives of the error, the kinematic equation is differentiated with respect to time, and the dynamic equation is substituted into the expression as follows:

$$\begin{aligned} \ddot{q} &= \frac{\partial f}{\partial q}\dot{q} + \frac{\partial f}{\partial \omega}\dot{\omega} \\ &= \frac{\partial f}{\partial q}\dot{q} + \frac{\partial f}{\partial \omega}[g(q, \omega, p) + h(\sigma, \omega, p)u + H(q, \omega)] \end{aligned} \tag{5.24}$$

Now that expressions for q, $\dot{q}$, and $\ddot{q}$ are available, with q_r, $\dot{q}_r$, $\ddot{q}_r$ prescribed, they can be substituted into the error dynamics equation to obtain:

$$\frac{\partial f}{\partial q}\dot{q} + \frac{\partial f}{\partial \omega}[g(q, \omega, p) + H(q, \omega) + h(\sigma, \omega, p)u] - \ddot{q}_r + C(\dot{q} - \dot{q}_r) + K(q - q_r) = 0 \tag{5.25}$$

For the specific case of the Mars ellipsled, the terms in the equation above are defined

as follows:

$$\frac{\partial f}{\partial \omega} = A(q) \tag{5.26}$$

$$\frac{\partial f}{\partial q} = \begin{pmatrix} 2\omega_1 q_1 & \omega_2 q_2 & \omega_3 q_3 \\ \omega_1 q_2 & 2\omega_2 q_2 & \omega_3 q_2 \\ \omega_1 q_3 & \omega_2 q_3 & 2\omega_3 q_3 \end{pmatrix} \tag{5.27}$$

$$h = [I]^{-1} \tag{5.28}$$

$$H = \omega \times I\omega \tag{5.29}$$

$$g = \frac{1}{2}\rho v^2 S_{ref} l_{ref} \begin{pmatrix} \frac{c_{l_\beta}\beta}{I_x} \\ \frac{c_{m_\alpha}\alpha}{I_y} \\ \frac{c_{n_\beta}\beta}{I_z} \end{pmatrix} \tag{5.30}$$

where S_{ref} is the vehicle reference area, l_{ref} is the reference length, and c_{l_β}, c_{m_α}, and c_{n_β} are aerodynamic coefficients. The g term contains both known and unknown parameters, and it is crucial to separate them. The most critical unknown parameter for the Mars entry problem is the atmospheric density, ρ. Additionally, the aerodynamic coefficients are typically highly uncertain, and g contains both of these parameters. The controller gains are specifically designed to adapt for this lack of knowledge. The g term can be rewritten as follows.

$$g = \frac{1}{2}v^2 S_{ref} l_{ref} [I]^{-1} \begin{pmatrix} \beta & 0 & 0 \\ 0 & \alpha & 0 \\ 0 & 0 & \beta \end{pmatrix} \rho \begin{pmatrix} c_{l_\beta} \\ c_{m_\alpha} \\ c_{n_\beta} \end{pmatrix} \tag{5.31}$$

This expression can also be written as $g = GL$ where G contains the known parame-

ters and L contains the unknown parameters.

$$G = \frac{1}{2}V^2 S_{ref} l_{ref} [I]^{-1} \begin{pmatrix} \beta & 0 & 0 \\ 0 & \alpha & 0 \\ 0 & 0 & \beta \end{pmatrix} \tag{5.32}$$

$$L = \rho \begin{pmatrix} c_{l_\beta} \\ c_{m_\alpha} \\ c_{n_\beta} \end{pmatrix} \tag{5.33}$$

However, the density is an explicit function of the altitude. An adaptive controller works well with an adaptation law that is updated faster than the dynamics of the system. In this case, the density is a function of the altitude which changes rapidly with time. To avoid this problem, the density, which is typically an exponential model, is instead expressed as a power series in h:

$$\rho = \mathbf{f}(h)^T \ \mathbf{\Theta} \tag{5.34}$$

where the know vector $\mathbf{f}(h)$ and the unknown parameter vector $\mathbf{\Theta}$ are expressed as

$$\mathbf{f}(h) = [1 \ h \ h^2 \ h^3 \ h^4 \ ...]^T \tag{5.35}$$

$$\mathbf{\Theta} = [\Theta_0 \ \Theta_1 \ \Theta_2 \ \Theta_3 \ \Theta_4 ...]^T \tag{5.36}$$

Since the density is now separated into known and unknown vectors, the terms G and L can be redefined as:

$$G = \frac{1}{2}V^2 S_{ref} l_{ref} [I]^{-1} \begin{pmatrix} \beta & 0 & 0 \\ 0 & \alpha & 0 \\ 0 & 0 & \beta \end{pmatrix} \mathbf{f}^T(H) \tag{5.37}$$

$$L = \mathbf{\Theta} \begin{pmatrix} c_{l_\beta} \\ c_{m_\alpha} \\ c_{n_\beta} \end{pmatrix} \tag{5.38}$$

Expressions for all terms in the error dynamics equation have been derived. It is now possible to solve for the control law u:

$$\begin{aligned} u &= -\left(\frac{\partial f}{\partial \omega}\,[I]^{-1}\right)^{-1}\left[\frac{\partial f}{\partial \omega}(GL+H) + \frac{\partial f}{\partial q}\dot{q} - \ddot{q}_r + C(\dot{q}-\dot{q}_r) + K(q-q_r)\right] \\ &= -[I]\left[GL + \frac{\partial f}{\partial \omega}^{-1}\left(\frac{\partial f}{\partial \omega}H + \frac{\partial f}{\partial q}\dot{q} - \ddot{q}_r + C(\dot{q}-\dot{q}_r) + K(q-q_r)\right)\right] \end{aligned} \tag{5.39}$$

To simplify the expression above, the control law is written as follows.

$$u = -[I](GL + \Psi) \tag{5.40}$$

where Ψ is defined as follows.

$$\Psi = \frac{\partial f}{\partial \omega}^{-1}\left(\frac{\partial f}{\partial \omega}H + \frac{\partial f}{\partial q}\dot{q} - \ddot{q}_r + C(\dot{q}-\dot{q}_r) + K(q-q_r)\right) \tag{5.41}$$

The control law in equation 5.40 requires knowledge of L and I, so adaptive laws will be developed for each. The true values of L and I are defined as L^* and I^*, and their estimates as $L(t)$ and $I(t)$. Adaptation laws will be developed for the difference between the true and the estimated values of each parameter, and these are defined as:

$$\widetilde{L} = L(t) - L^* \tag{5.42}$$

$$\widetilde{I} = I(t) - I^* \tag{5.43}$$

The control identity is defined as $GL + \Psi + I^{-1}u = 0$. Adding and subtracting the control identity for the known and unknown parameter cases to the error dynamics

equation, the following is obtained:

$$\ddot{e} + C\dot{e} + Ke = GL + \Psi + I^{-1}u - GL^* - \Psi - I^{*-1}u \tag{5.44}$$

$$\ddot{e} = -C\dot{e} - Ke + G\widetilde{L} + \widetilde{I}^{-1}u \tag{5.45}$$

A candidate Lyapunov function for the design of the adaptation laws is given by equation 5.46. It is positive definite. The first and second terms contain the bank angle error and its derivative. The third and fourth terms will yield adaptive laws for L and $\mathcal{I}$ in subsequent steps of this derivation.

$$V = \frac{1}{2}\dot{e}^T\dot{e} + \frac{1}{2}e^TKe + \frac{1}{2}\widetilde{L}^T\Gamma_1^{-1}\widetilde{L} + \frac{1}{2}Tr[\widetilde{\mathcal{I}}^T\Gamma_2^{-1}\widetilde{\mathcal{I}}] \tag{5.46}$$

Let $\widetilde{I}^{-1}$ be redefined as $\widetilde{\mathcal{I}}$ for convenience of notation. The time derivative of the Lyapunov function is given by:

$$\begin{aligned}
\dot{V} &= \dot{e}^T\ddot{e} + \dot{e}^TKe + \widetilde{L}^T\Gamma_1^{-1}\dot{\widetilde{L}} + Tr[\widetilde{\mathcal{I}}^T\Gamma_2^{-1}\dot{\widetilde{\mathcal{I}}}] \\
&= -\dot{e}^T(C\dot{e} + Ke) + \dot{e}^T(G\widetilde{L} + \widetilde{\mathcal{I}}u) + \dot{e}^TKe + \widetilde{L}^T\Gamma_1^{-1}\dot{\widetilde{L}} + Tr[\widetilde{\mathcal{I}}^T\Gamma_2^{-1}\dot{\widetilde{\mathcal{I}}}] \\
&= -\dot{e}^TC\dot{e} + (\dot{e}^TG\widetilde{L} + \widetilde{L}\Gamma_1^{-1}\dot{\widetilde{L}}) + (\dot{e}^T\widetilde{\mathcal{I}}u - \widetilde{\mathcal{I}}^T\Gamma_2^{-1}\dot{\widetilde{\mathcal{I}}})
\end{aligned} \tag{5.47}$$

The derivative of the Lyapunov function must be negative semidefinite. To achieve this, the second and third terms of equation 5.47 are set to zero. This yields the following adaptive laws for L and I:

$$\dot{\widetilde{L}} = -\Gamma_1G^T\dot{e} \tag{5.48}$$

$$\dot{\widetilde{\mathcal{I}}} = -\Gamma_2u\dot{e}^T \tag{5.49}$$

To summarize, the adaptive laws for the density function coefficients and aerodynamic coefficients, and for the inverse of the inertia matrix are given in equations 5.48 and 5.49, respectively. The adaptation rate depends on the learning rates, Γ_1

and Γ_2. These laws do not guarantee parameter estimate convergence; they can only guarantee error convergence.

CHAPTER VI

EXPERIMENT DESIGN

This chapter outlines the experiment used to evaluate the feasibility of applying two adaptive control systems to the Mars entry problem, and to evaluate their performance during Mars atmospheric flight for the ellispled.

A. Entry Interface Conditions

The scope of this research is limited to the control design during atmospheric flight from the entry interface point at approximately 125 kilometers above the surface of the planet until the deployment of the parachute at approximately 12 kilometers of altitude. The entry interface, or initial conditions, used for the simulation were taken from the previous study on the ellispled [1]. These conditions are the following:

- Entry velocity of 7.3 km/s
- Altitude 125 km
- Flight path angle -10 degrees
- Initial bank angle 80 degrees

B. Entry Trajectory

As mentioned previously, the controllers track a series of bank angle commands for a time period of approximately 350 seconds. A flight time of 350 seconds was used for this simulation because, based on previous results [1], it is the length of time required for the ellipsled to fly from the entry interface point at 125 km to an altitude of 12 km, which is approximately when the parachute is deployed.

The goal of this thesis is to demonstrate the ability of the adaptive controllers to follow realistic bank maneuvers throughout the flight. An arbitrary series of bank angle commands of various magnitudes were chosen to test the controllers. This trajectory was chosen to maintain the vehicle on an altitude profile such that it flies from 125 kilometers above the surface to an altitude of approximately 12 kilometers in a period of 350 seconds. Additionally, the mathematics behind the development of both control laws require a smooth trajectory. To satisfy this requirement, the step commands were reshaped to obtain a differentiable reference signal. This was done by fitting a fifth order polynomial for each step command.

C. Controller Evaluation

The goal is to evaluate the feasibility and performance of an adaptive control system for a Mars entry vehicle. More specifically, the following questions need to be answered:

- What are the limitations of adaptive control for the Mars entry problem?
- How does an adaptive control system respond to rapid changes in the atmospheric conditions?
- How well does the adaptive controller perform under the presence of uncertainties in the mass and inertia values in addition to the uncertainties in the environment?
- Is the controller robust enough to handle large initial position and velocity errors?
- How fast can the bank reversals occur and still give the controller enough time to learn and perform well?

- How large can the bank angle commands be in order for the adaptive controller to perform well?

To compare the two controllers, each was tuned individually for the best possible performance without any vehicle or environment model uncertainties. The body rates are taken into account for selecting the controller gains. The maximum control input within reaction control system jets capabilities, shown in Table V is also considered, as well as the frequency of oscillation of the control input signal. Additionally, the response time and settling time for a given step command was evaluated.

Table V. Maximum Control Input

Axis	Magnitude	Units
Roll	315	$N \cdot m$
Pitch	498	$N \cdot m$
Yaw	854	$N \cdot m$

1. Step Response Evaluation

Each of the controllers are evaluated for a set of step commands as well as for the entry trajectory previously mentioned. The goal is to determine their performance limits by analyzing how each controller can handle uncertainties in both the vehicle properties and the atmospheric density. The bank angle step commands used to test the controllers are of different magnitudes. Each command is also tested for different time intervals. This is done to determine the performance of each controller for each of the maneuvers and the amount of control input required of each bank maneuver. In addition, a maximum bank angle command of 170° is tested with

the maximum control input to determine the minimum time in which each of the controllers can track such a bank angle command. The same tests are repeated for cases with uncertainties in the density and aerodynamic coefficients, cases with uncertainties in vehicle properties, and cases with uncertainties in all parameters mentioned above.

2. Entry Trajectory Tracking Evaluation

Both controllers are evaluated while tracking the smooth entry trajectory mentioned previously. The simulations will be run for cases that contain uncertainties in the density and aerodynamic coefficients, uncertainties in the vehicle inertias, and a combination of both. The performance measures used to evaluate these results will be the control energy and control effort, as well as the integral square error and the integral square error multiplied by time of the attitude.

CHAPTER VII

RESULTS

This section contains the simulation results from the cases discussed in the previous chapter. Results are presented for the MRAC controller, the SAMI controller, and a comparison between both control systems for the Mars entry problem.

A. MRAC

The values for the tuning parameters were selected based on the performance of the controller while tracking the aforementioned smooth entry trajectory. The control law is given by $u = \widetilde{a}_r \omega_r + \widetilde{a}_\omega \omega$ where the gains $\widetilde{a}_r$ and $\widetilde{a}_\omega$ are adaptive. Their adaptation equations require an initial value and a learning rate. The learning rate was selected as $\Gamma = 1 \times 10^5$ to minimize the control input. The initial gain values were selected as

$$\widetilde{a}_r(0) = \widetilde{a}_\omega(0) = \begin{bmatrix} 1 \times 10^3 & 0 & 0 \\ 0 & 1 \times 10^3 & 0 \\ 0 & 0 & 1 \times 10^4 \end{bmatrix} \tag{7.1}$$

based on the average value of the gains throughout the simulation.

It is important to point out that the basic MRAC control system developed here defines the error as $e = \omega - \omega_r$. The derivation of the adaptive laws guarantees convergence of the angular velocities, but it does not guarantee convergence of attitude error or unknown parameter estimates.

1. Step Response for MRAC Controller

This section presents results for the step response of the basic MRAC controller. One of the goals of this research is to determine the limits under which an adap-

tive control system performs well. To test the capabilities of the controller, several bank angle commands were evaluated. Entry vehicles such as the ellipsled can theoretically roll about the velocity vector as much as they need to. For this problem, the largest bank command was chosen to be 170°, which translates into having the vehicle oriented such that the lift vector, **L**, is almost pointing towards the ground. This bank angle was commanded in several time intervals; it was determined that the fastest time interval in which the ellipsled can perform this maneuver without exceeding the available control input limits is approximately 10 seconds. Figure 11 shows the tracking performance of the MRAC controller for a bank angle command of 170°. Clearly, there is a steady state error because, as mentioned previously, the MRAC controller guarantees convergence of the angular velocity error but not of the attitude error. Figure 12 shows the control input required to perform this maneuver. The magnitudes of the control input signals for each axes are within the RCS jet capabilities.

2. Effects of Uncertainties on the MRAC Controller

One of the main differences between the basic MRAC and SAMI is that MRAC cannot directly estimate unknown system parameters. The gains vary with the angular velocity error, and their values are not based on attitude error convergence nor unknown parameter estimates. This means that the adaptation mechanism does not depend directly on parameter estimation errors, and it is not possible to explicitly test the controller for a given amount of uncertainty in the system parameters. For example, making a comparison between a case with 50% density uncertainty and a case with 90% density uncertainty would only show that the controller gains reach different steady state values after a given period of time, but the performance of the system is approximately the same.

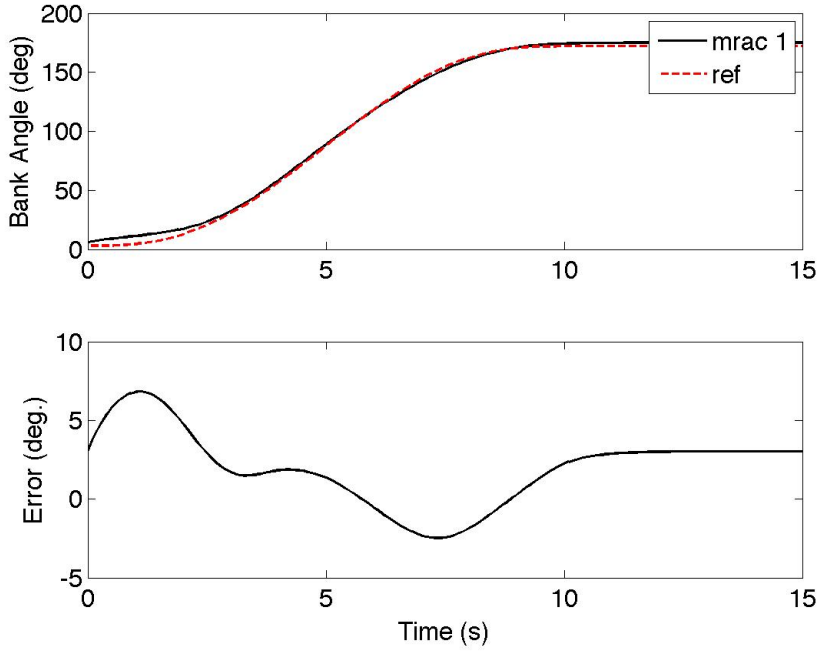

Fig. 11. MRAC: Maximum Bank Angle Command

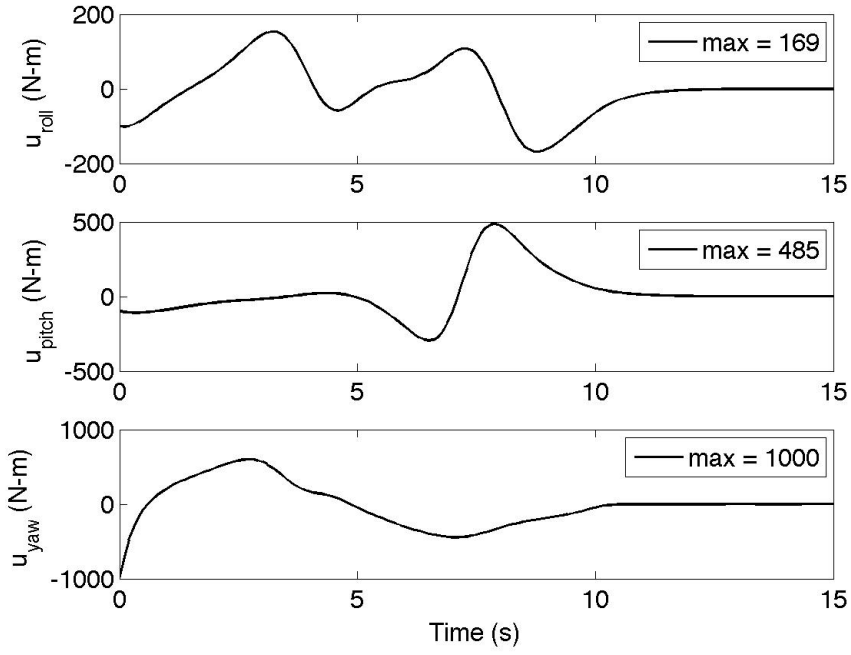

Fig. 12. MRAC: Maximum Control Input

3. Trajectory Tracking Performance of MRAC Controller

This section presents the results for tracking the entry trajectory mentioned previously. As seen in Figure 13, there is a steady state error present during most of the simulation time. This is due to the fact that MRAC guarantees angular velocity error convergence but not necessarily attitude error convergence. Even though the learning rates for an MRAC controller are not difficult to tune, it is challenging to find a set of learning rates that yields hight levels of performance throughout an entire entry trajectory. Towards the end of the simulation, it can be observed that there is a larger error. This is a result of the atmospheric density changing faster than the controller gains.

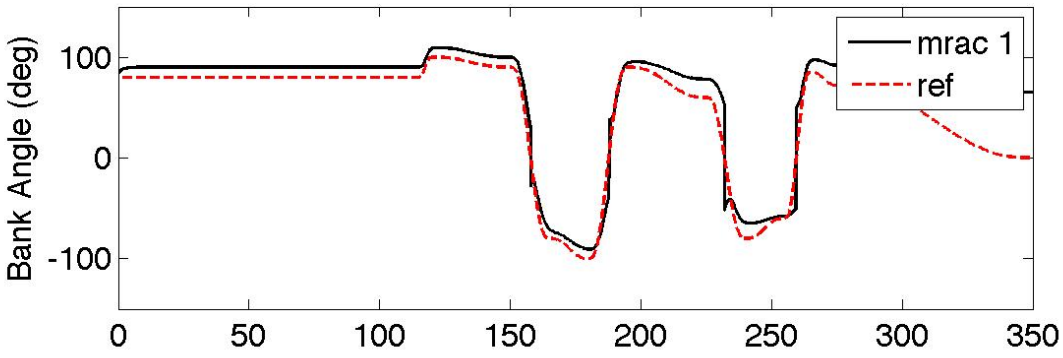

Fig. 13. MRAC: Bank Angle Tracking

B. SAMI

This section presents simulation results using the SAMI control system. As mentioned previously, SAMI adapts for unknown system parameters explicitly, but it does not guarantee convergence to the true values. The unknown parameters change with time only until error convergence is achieved. The tuning parameters for this controller are selected based on performance while tracking a smooth trajectory. These parameters

are the error dynamics gains, C and K, the initial values for $\mathcal{I}$ and L, and the learning rates Γ_1 and Γ_2 from equations 5.48 and 5.49 respectively. The error dynamics gains were selected as $C = 0.1 \cdot I_{3\times3}$ and $K = 10 \cdot I_{3\times3}$. The initial estimates for the inertias were selected as 80% of the true values. The initial estimates for the L vector were selected as zeros because this vector is composed of the aerodynamic coefficients and the atmospheric density function coefficients which are all small numbers.

The learning rates were selected as $\Gamma_1 = 1 \times 10^2 \cdot I_{6\times6}$ and $\Gamma_2 = 1 \times 10^{-5} \cdot I_{3\times3}$. Selecting the learning rates for the SAMI controller was a difficult task. There are several possible combinations of learning rates that can work for various magnitudes of step commands. However, finding the appropriate combination of learning rates for both the unknown parameter vector L and the inverse of the inertia matrix $\mathcal{I}$ required several iterations. In general, the process consisted of running several step commands for different points in the trajectory. Different step commands for various dynamic pressures were evaluated until an appropriate combination of learning rates was obtained. Adapting for the inverse of the inertia matrix required small learning rates because these parameters are very small. Higher learning rates caused high frequency oscillations in the estimates which translated into high frequency oscillations in the control input signal. On the other hand, adapting for the unknown parameter vector L required a fast learning rate. The density varies rapidly throughout the flight so its estimates must also change fast.

1. Step Response for SAMI Controller

The controller was tested under different scenarios to determine the effects of uncertainties in the atmospheric density as well as errors in the vehicle inertias and aerodynamic coefficients. The sections below describe these effects on the SAMI controller by looking at step responses. The goal is to find the largest bank command

that the SAMI controller can track in the least amount of time. The simulation had an initial bank angle error of three degrees in all cases. It was determined that the SAMI controller can track a bank angle of 170° in approximately 12 seconds without exceeding the control input limits. Figure 14 shows the commanded maneuver as well as the bank angle error. The tracking error quickly goes to zero and satisfactory tracking is achieved in less than ten seconds. Figure 15 shows that the control input is within the RCS jet limitations presented on Table V.

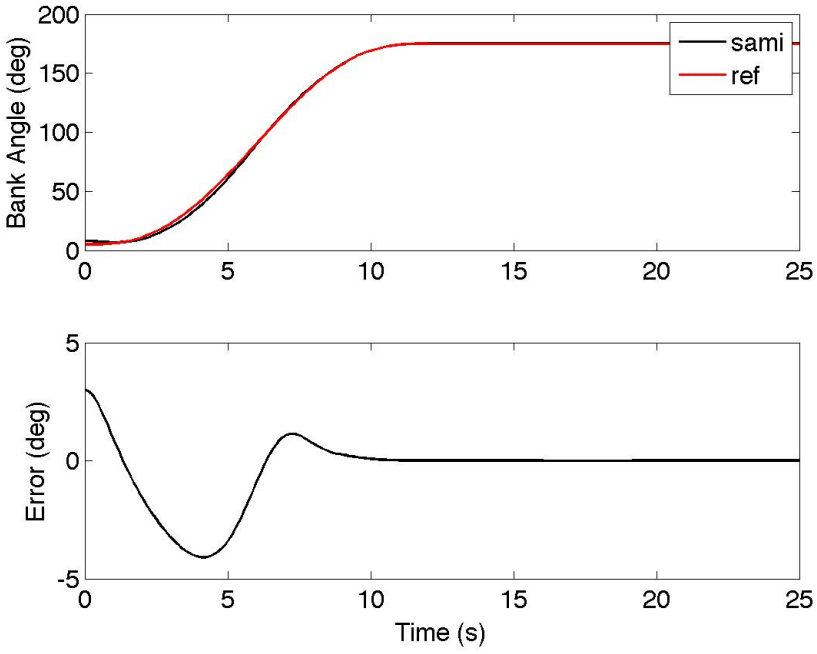

Fig. 14. SAMI: Maximum Bank Angle Command

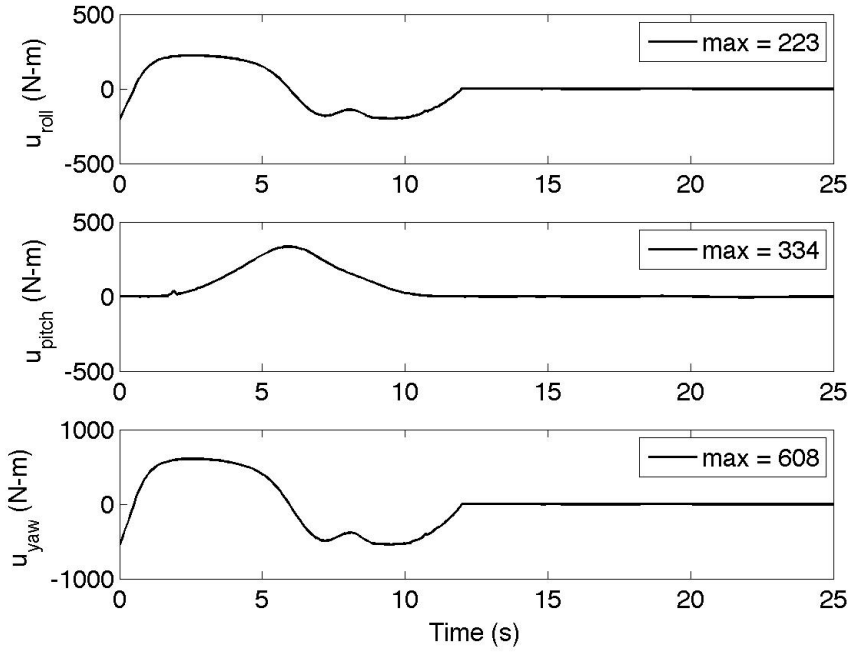

Fig. 15. SAMI: Maximum Control Input

2. Effects of Uncertainties on the SAMI Controller

The figures below show the effects of uncertainties in the atmospheric density, the vehicle inertias and aerodynamic coefficients, and the effect of all of these combined.

a. Effects of Uncertainty in Atmospheric Density and Aerodynamic Coefficients

Two cases were evaluated to determine the effects of density uncertainties. In the first case the controller uses the true density. In the second case, the control law has no knowledge of the true density. Instead, it uses the estimates of the unknown parameter vector to approximate a density function throughout the simulation. The figures below show that SAMI performs well under both scenarios. Figure 16 shows the tracking performance for both cases. The controller has a similar performance for both cases in terms of error convergence. Figure 17 shows control inputs required for this maneuver. The roll and yaw signals are similar in magnitudes. However, the pitch control input is significantly higher for the case with unknown density and aerodynamic coefficients. This is due to the fact that the pitching moment coefficient is much more sensitive to errors than the rolling and yawing coefficients since the equations of motion were developed under the assumption that the vehicle remains trimmed in pitch.

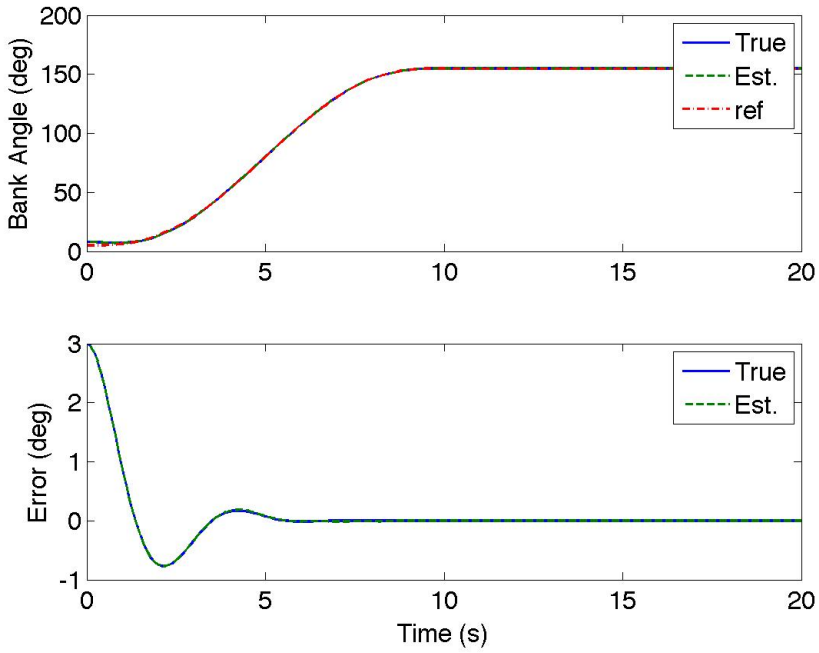

Fig. 16. SAMI: Bank Angle - Uncertainties in Aerodynamic Coefficients, and Density

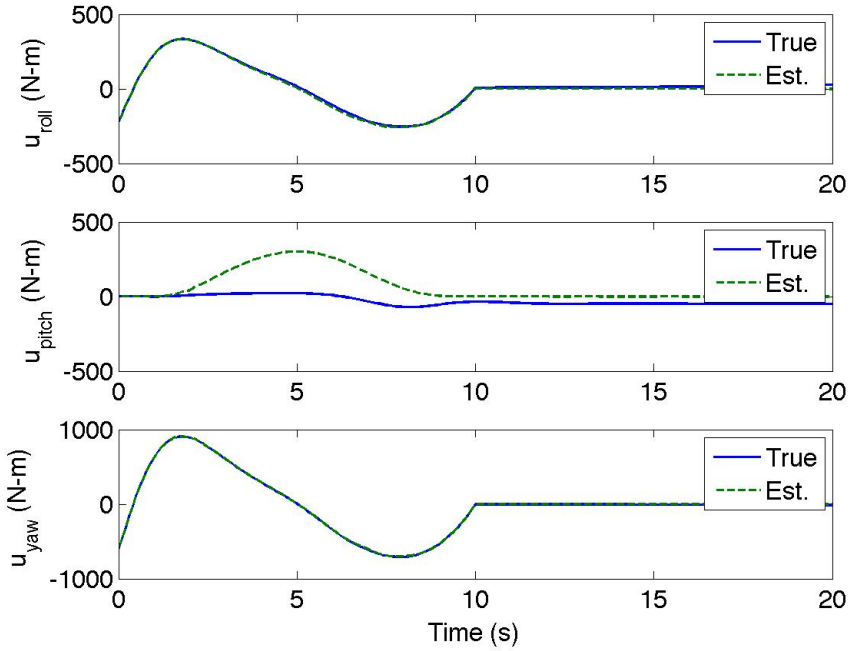

Fig. 17. SAMI: Control Input - Uncertainties in Aerodynamic Coefficients, and Density

b. Effects of Uncertainty in the Vehicle Inertias

A similar test was performed to determine the effects of errors in the inertia and aerodynamic coefficients. As mentioned in the control design section of this thesis, the SAMI controller estimates the inverse of the inertia matrix $[I]^{-1}$. The simulation was run for both cases where the true inertia values and the inertia estimates are used. Figures 18 and 19 show that the controller performs well in both scenarios. The bank angle error as well as the control input signals are of comparable magnitudes. The main difference between the two cases is the initial oscillation in the control input signal due to the estimation of the inertias. Once the inertia values have settled as seen in Figure 20, the control input signal is as smooth as it is in the case where the controller has full knowledge of the true inertias.

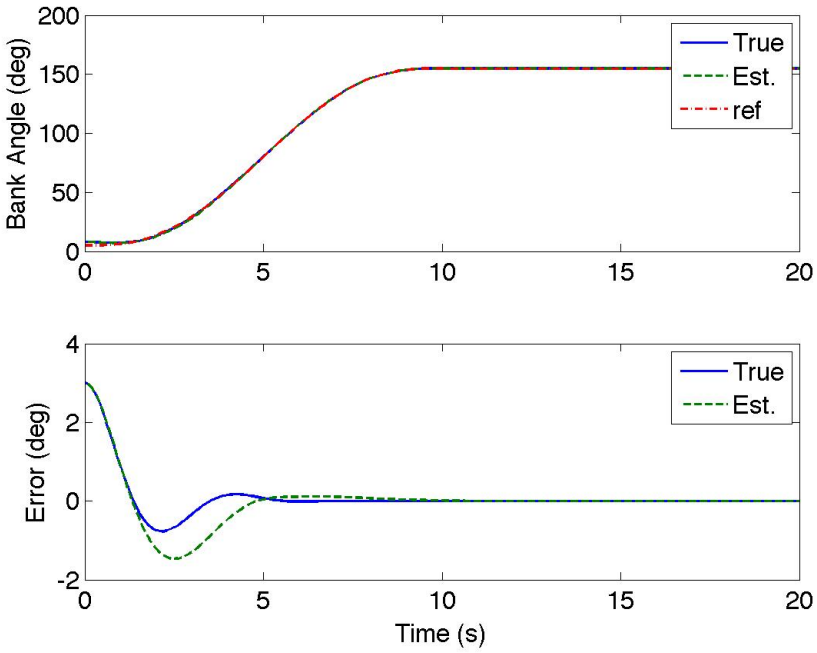

Fig. 18. SAMI: Bank Angle - Uncertainties in Inertias

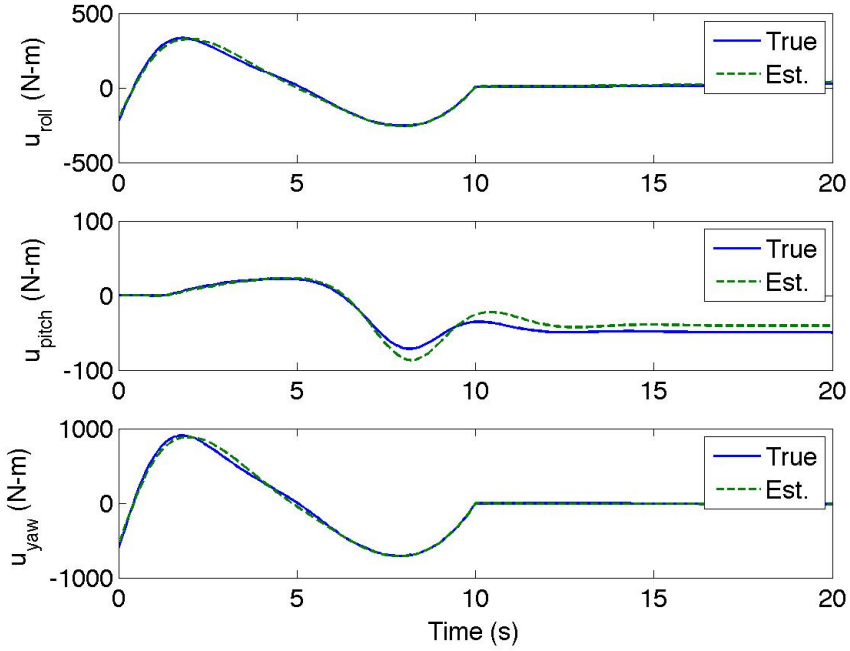

Fig. 19. SAMI: Control Input - Uncertainties in Inertias

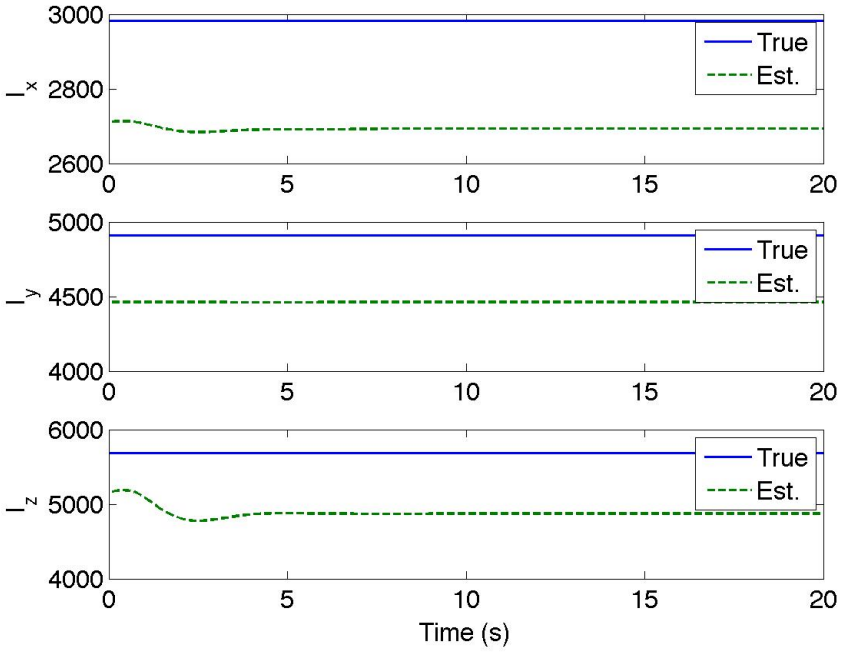

Fig. 20. SAMI: Inertia Estimates - Uncertainties in Inertias

c. Effects of Uncertainties in Density, Aerodynamic Coefficients, and Vehicle Inertias

Figures 21 - 23 compare a case where the controller has knowledge of all parameters to a case where the controller uses uncertain parameters. These results demonstrate that the SAMI controller can perform well without having knowledge of the vehicle inertias, aerodynamic coefficients, or atmospheric density. Both cases were simulated with an initial bank angle error of 3°. As expected, the error converges faster for the case in which the controller has full knowledge of all parameters. The control input for all axes are of comparable magnitude for both cases. Figure 23 shows the time history of the estimates of the vehicle inertias. These values do not converge to the true values. Instead, they settle to a constant value as soon as bank angle error convergence is achieved.

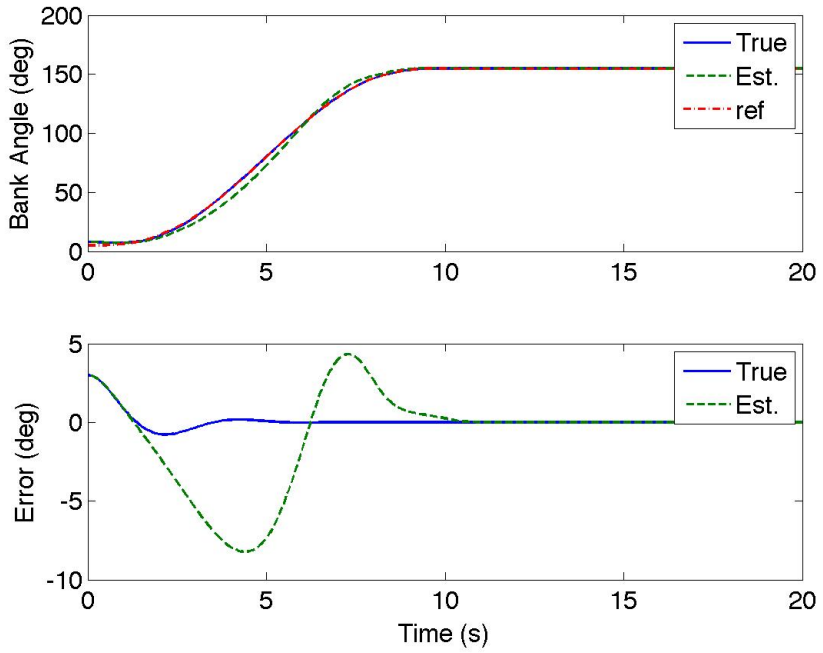

Fig. 21. SAMI: Bank Angle - Uncertainties in Inertias, Aerodynamic Coefficients, and Density

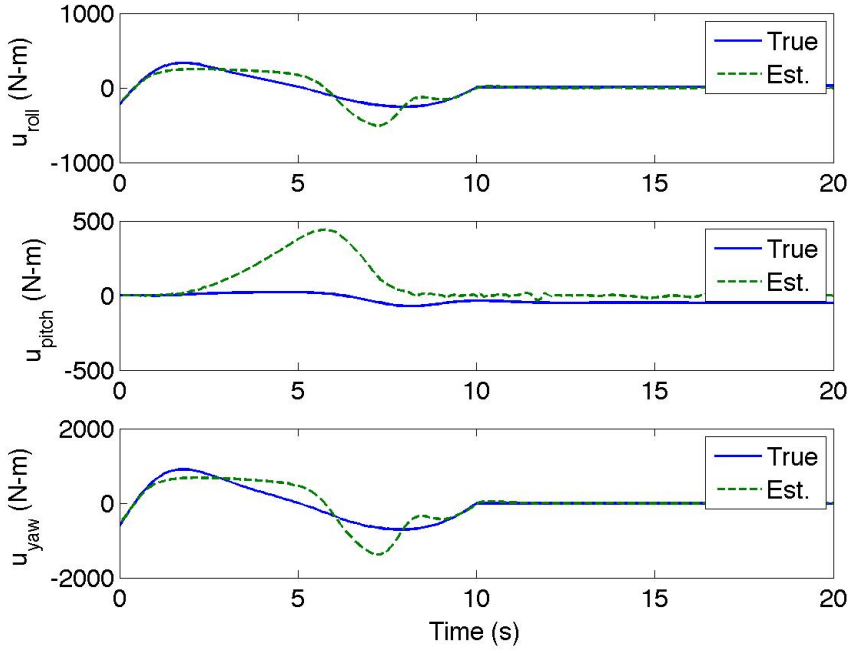

Fig. 22. SAMI: Control Input - Uncertainties in Inertias, Aerodynamic Coefficients, and Density

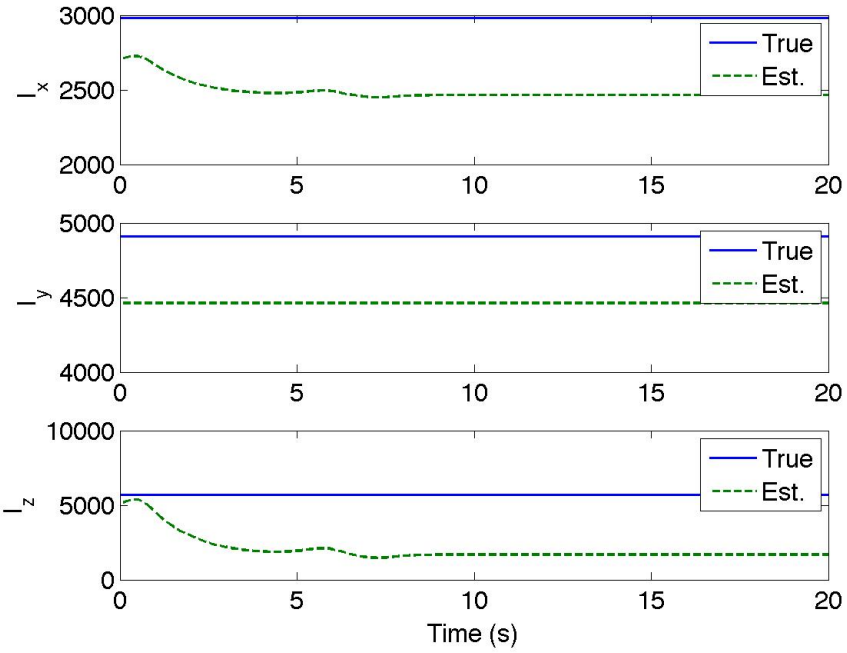

Fig. 23. SAMI: Inertia Estimates - Uncertainties in Inertias, Aerodynamic Coefficients, and Density

3. Trajectory Tracking for SAMI Controller

Figures 24 through 29 show results for the SAMI control system tracking an entry trajectory. Figure 24 shows the bank angle tracking performance. An initial error of 3° converges quickly. There is an additional small error at approximately 260 seconds; this is due to the very steep command that the controller must track at this particular time. Figure 25 shows the control input required to follow the trajectory. The figure also shows the maximum control required at a given time. The yaw control input exceeds the limits by approximately 100 N at approximately 260 seconds. This again, is due to the very demanding maneuver that SAMI must track at this time. Figure 26 shows the angular velocities for the ellipsled which are all within limits. Figure 27 shows the time histories of the inertia values. Here, I_x and I_z take some time to converge to a constant value, whereas I_y is constant most of the time. This is because the vehicle is stable in pitch and the controller is mostly concerned with tracking maneuvers that involve rolling and yawing motions.

Figure 28 shows the inertial velocity of the ellipsled as well as the downrange and altitude with respect to the surface of the planet. As mentioned in the experiment design section of this thesis, the entry interface conditions include a velocity of 7.3 km/s and an altitude of 125 km. The velocity is drastically reduced as soon as the dynamic pressure peaks. As soon as the velocity magnitude decreases, the altitude rate also decreases as seen in the third plot on Figure 28. This effect can also be seen on Figure 29, where the flight path angle changes from a negative value to a positive value. This sign change occurs when the dynamic pressure peaks, or soon after, when the aerodynamic forces have a larger magnitude than the gravity force.

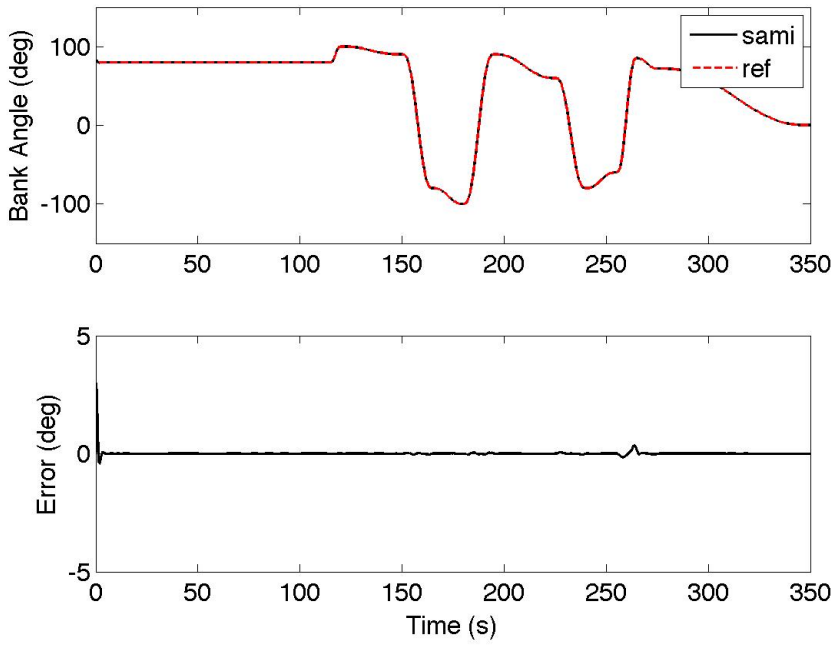

Fig. 24. SAMI: Bank Angle

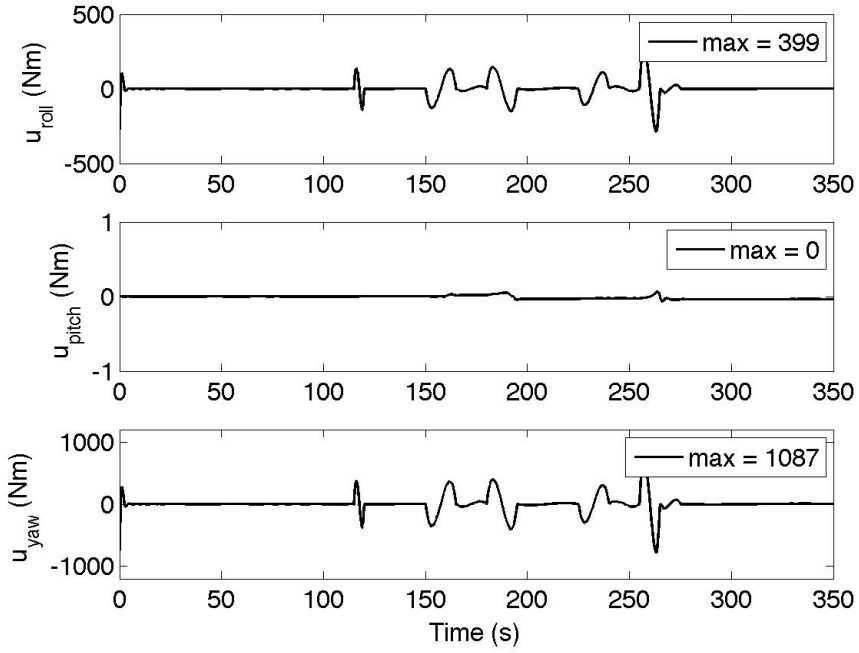

Fig. 25. SAMI: Control Inputs

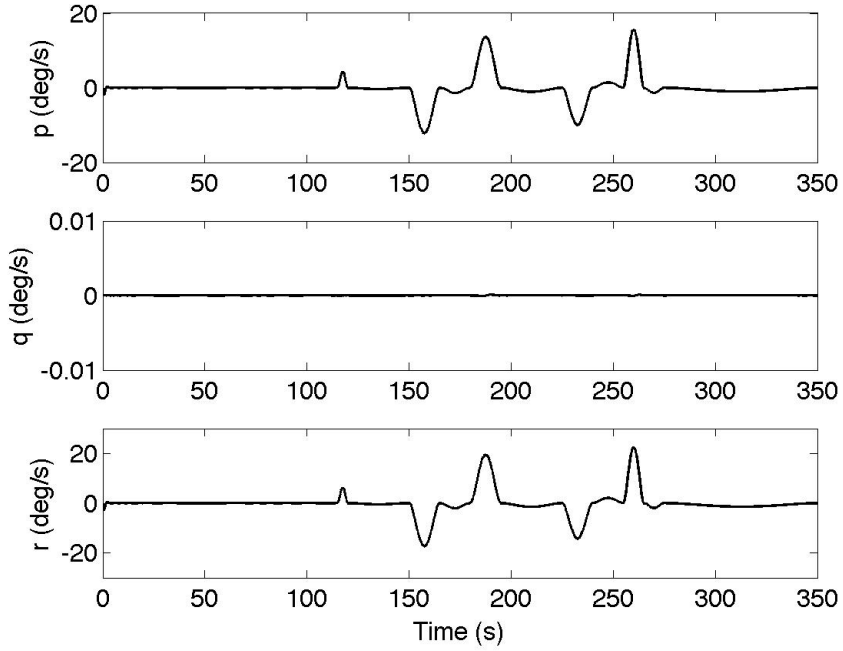

Fig. 26. SAMI: Angular Velocity

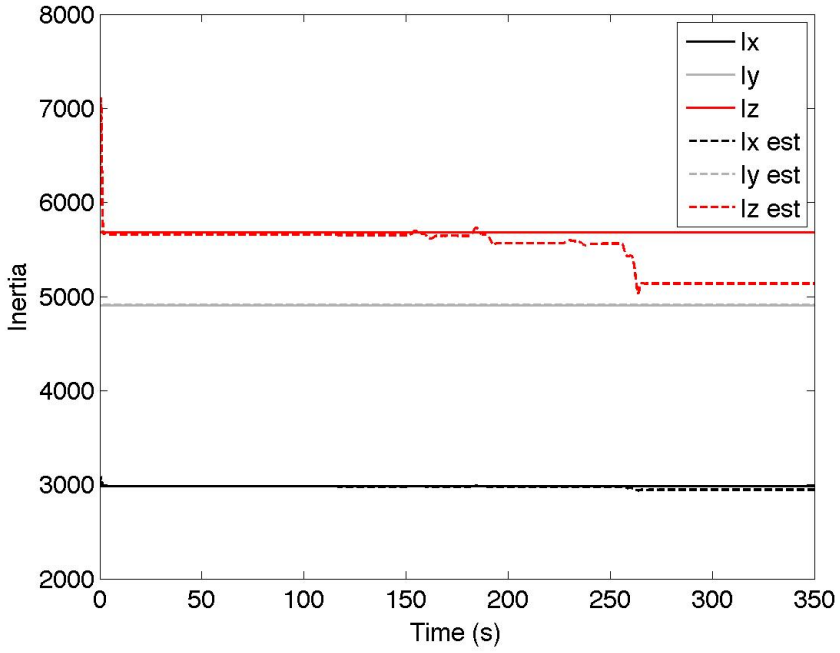

Fig. 27. SAMI: Inertia Estimates

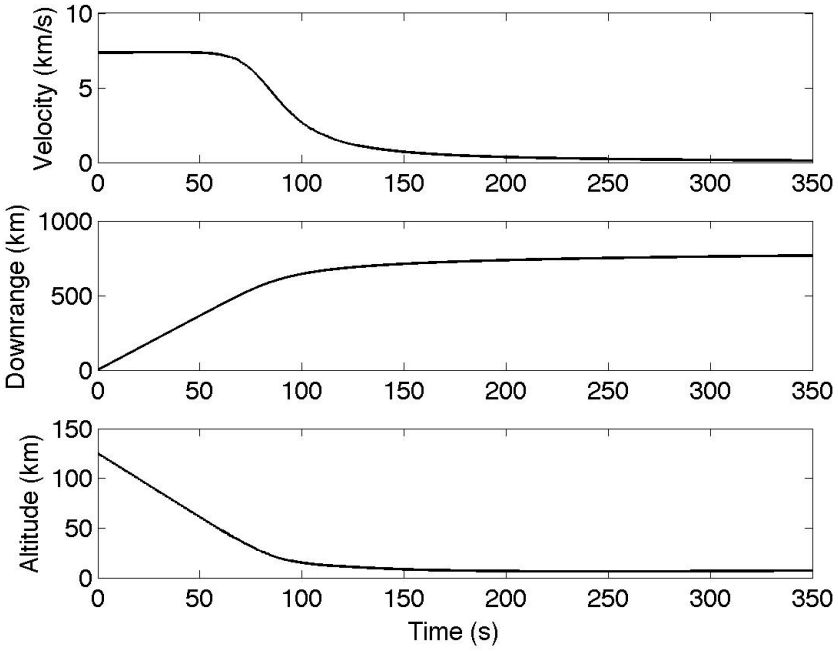

Fig. 28. SAMI: Inertial Velocity, Downrange, and Altitude

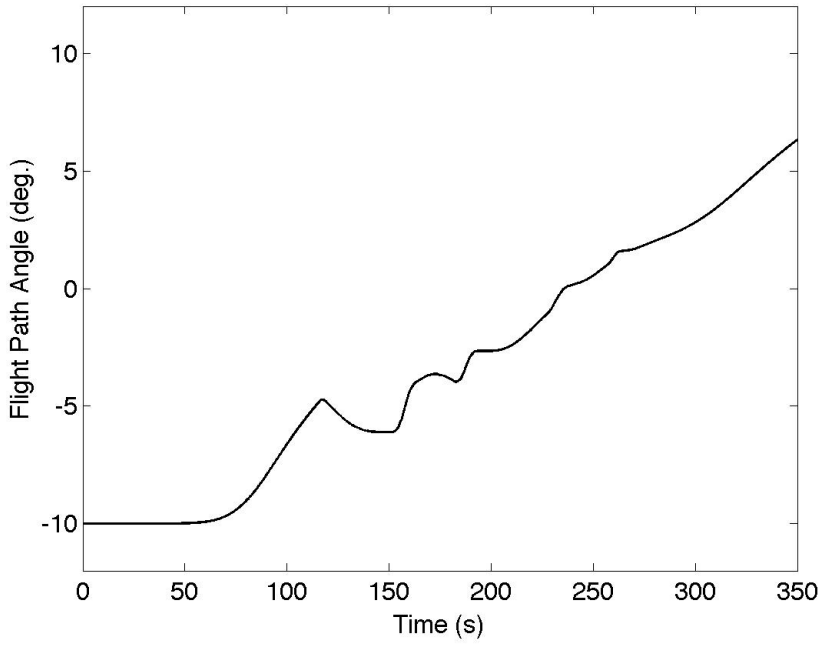

Fig. 29. SAMI: Flight Path Angle

The goal of this thesis was to design a controller that could provide satisfactory tracking performance during entry under the presence of atmosphere uncertainty as well as uncertainty in vehicle properties. Based upon the results shown here, SAMI appears to be capable of tracking a demanding entry trajectory. The controller is robust enough to operate without knowledge of atmospheric density, as well as with incorrect values of vehicle inertias and aerodynamic properties. The control requirements are within reasonable limits for all axes. However, in order to implement this system on a real flight vehicle, it will be necessary to re-evaluate the performance to ensure that the ellipsled will not exceed body rate limits or g-loads since it will be carrying a crew.

C. MRAC vs. SAMI

A comparison between the two adaptive control systems is presented in this section. Measures of performance for both controllers are discussed as well as the overall advantages and disadvantages of each controller.

1. Step Response

Figures 30 through 33 summarize the step response results for both controllers. It can be concluded from Figure 30 that SAMI has much better tracking performance than the MRAC approach. The error converges to zero rapidly whereas the error for the MRAC controller settles at a nonzero constant value. However, as Figure 31 shows, SAMI also requires more control input. As expected, higher performance requires greater control effort. Figure 32 shows the vehicle angular velocities. Both cases have velocities of comparable magnitudes and they all converge to zero in approximately 15 seconds. For the sake of completeness, Figure 33 shows the integral square error of

the bank angle in radians. However, these figures are misleading because the MRAC controller yields a steady state error, which accounts for the large difference in the accumulated error with time.

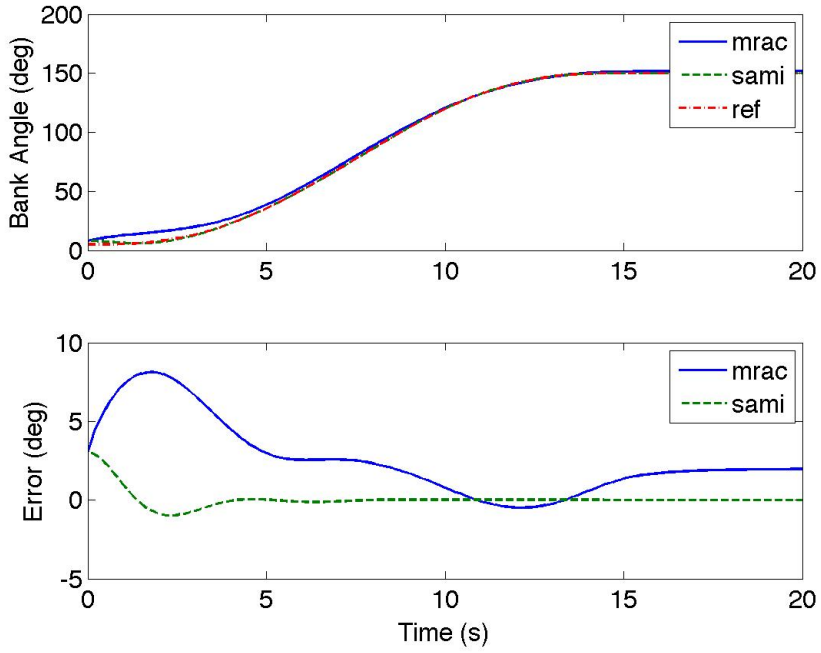

Fig. 30. MRAC vs. SAMI: Bank Angle

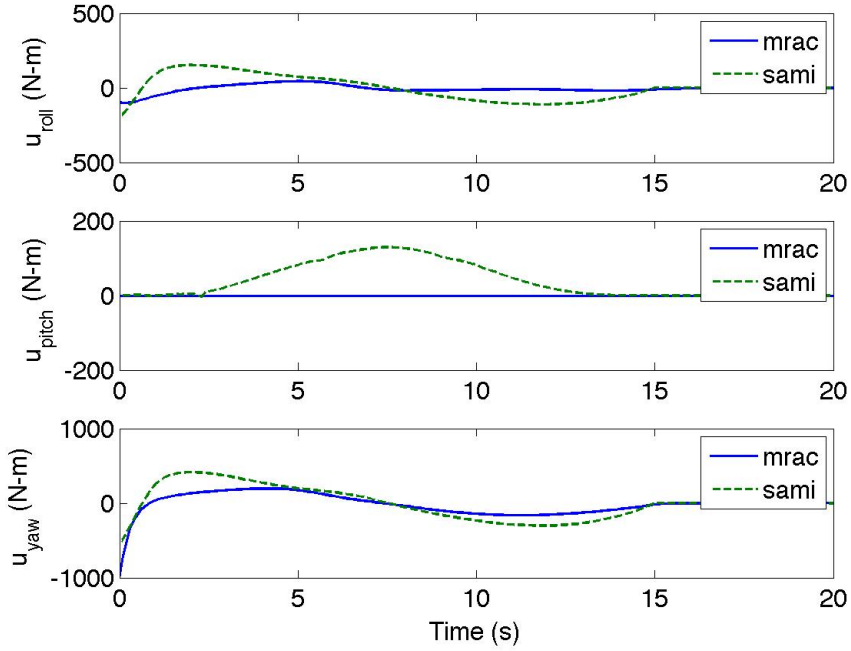

Fig. 31. MRAC vs. SAMI: Control Input

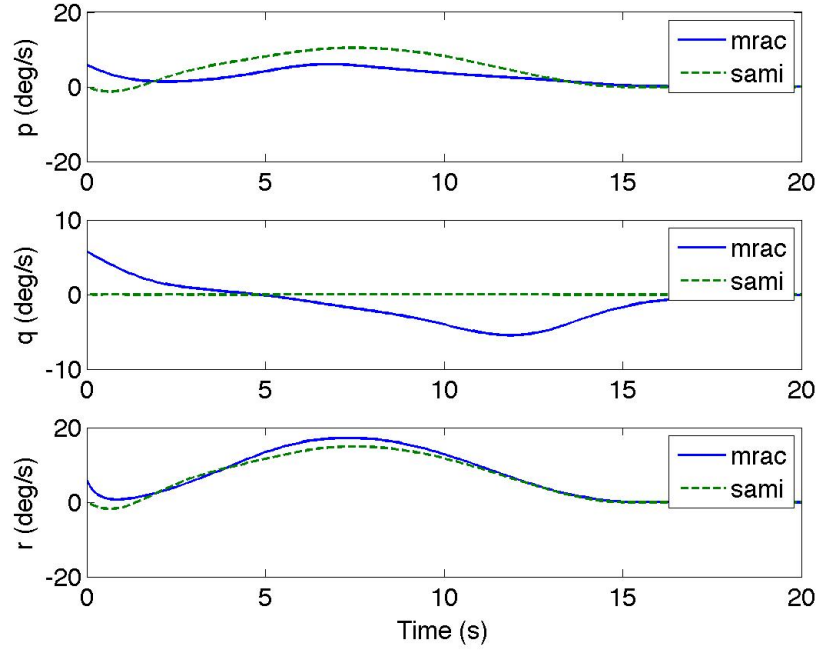

Fig. 32. MRAC vs. SAMI: Angular Velocity

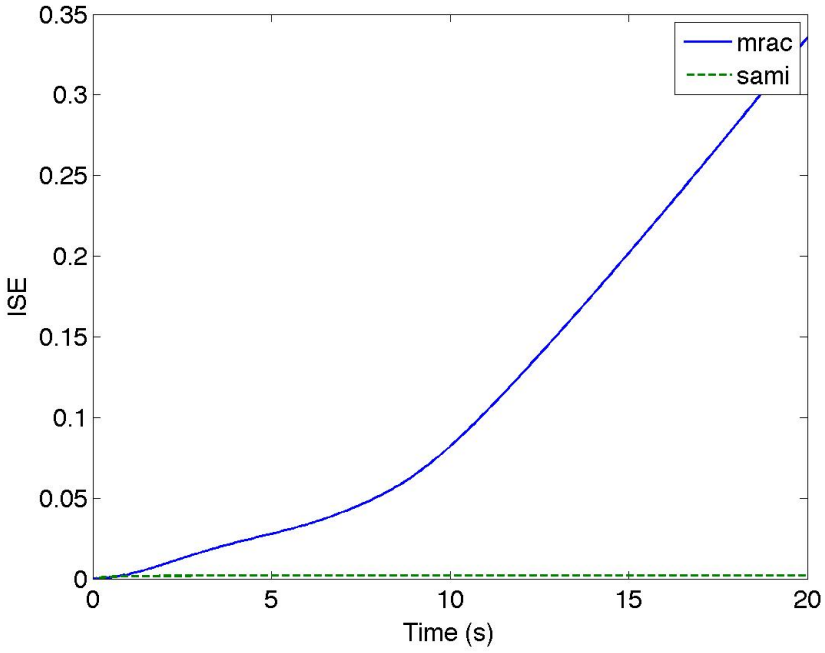

Fig. 33. MRAC vs. SAMI: Integral Square Error

2. Entry Trajectory Tracking

Additional performance measures for both control systems are presented in the figures below. Figure 34 shows the control effort defined as $u^T u$ for both MRAC and SAMI. This figure is a very good comparison of performance. It is important to notice that the peaks of both curves are at approximately the same level, indicating that the control effort of both controllers is of comparable magnitude. Figure 35 shows the control energy defined as $\int_{t_0}^{t} u^T u \; dt$. This is also an important result since it shows that even though both controllers have similar control effort, the control energy is significantly different. SAMI requires more control energy, but as mentioned previously, it has a much higher tracking performance.

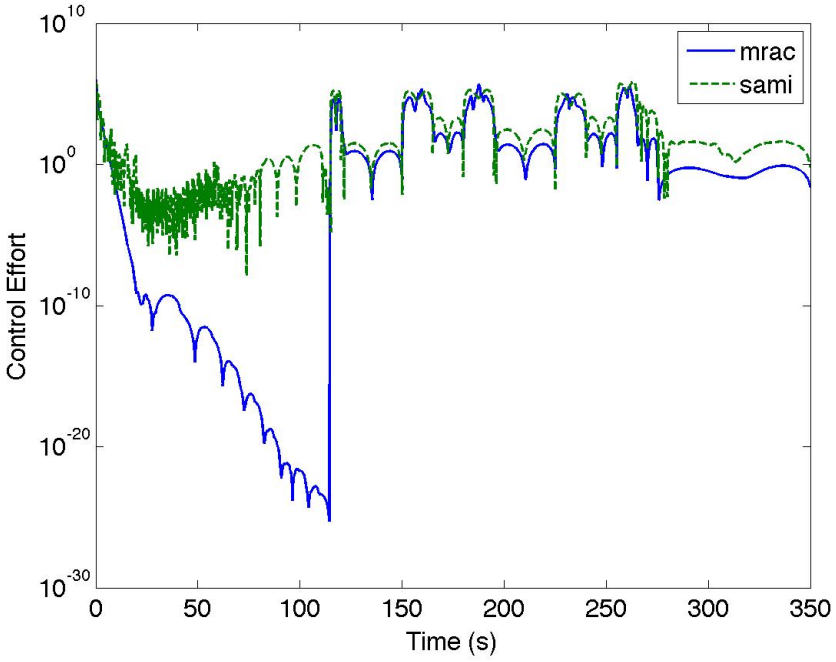

Fig. 34. MRAC vs. SAMI: Control Effort

To summarize the results presented in this section, it can be concluded that both controllers can perform well with uncertainties in the environment and vehicle model.

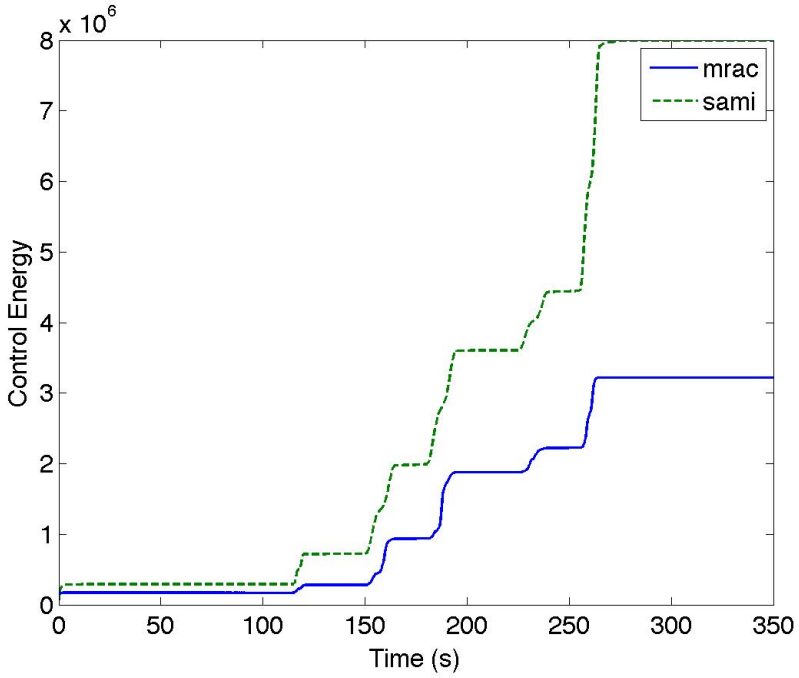

Fig. 35. MRAC vs. SAMI: Control Energy

It can also be stated that the SAMI controller has a higher level of performance. The tracking error converges to zero rapidly whereas for the MRAC controller, it does not. SAMI also requires more control input than MRAC and it is more difficult to tune and implement. An MRAC controller is not very sensitive to the gain values or learning rate; however, the SAMI controller is extremely sensitive to the magnitudes of the learning rates. In general, there is a trade-off between level of performance and higher control inputs and the level of difficulty in the implementation process.

CHAPTER VIII

CONCLUSIONS

Based on results presented in this thesis, the following conclusions are made.

1. For the entry control problem studied in this thesis, model reference adaptive control was capable of tracking bank angle commands up to 170° in approximately ten seconds, provided the trajectory is smooth. It was also possible to tune the learning rates and other parameters to obtain acceptable tracking performance during an entire entry trajectory.

2. Of the two model reference adaptive controllers designed and studied for this thesis, the SAMI controller provided better tracking performance than the MRAC controller because it specifically adapts for the lack of knowledge of atmospheric density, aerodynamic coefficients, and vehicle inertias. However, the SAMI controller also requires more control energy than the MRAC controller to track the same reference trajectory.

3. The basic MRAC controller was straightforward to design and implement and was judged useful for preliminary design and analysis. By comparison, the SAMI controller required more skill and experience to design due to the dynamical structuring and modeling aspects. Tuning of the SAMI controller was also more demanding due to sensitivity of the learning rates to atmospheric density and vehicle inertias. Since atmospheric density changes rapidly and the control law is an explicit function of the vehicle inertias, the controller is sensitive with respect to how fast these values can be estimated.

4. Based on the results presented in this thesis, SAMI is judged to be a promising candidate for a Mars entry vehicle controller. Results presented in this thesis

demonstrate the feasibility of SAMI controlling an entry vehicle without knowledge of atmospheric density or exact knowledge of vehicle properties such as inertias and aerodynamic coefficients.

CHAPTER IX

RECOMMENDATIONS

1. One of the most important and fundamental extensions to this research is to study guidance and adaptive control together. Since a real vehicle will have an active guidance system, it would be valuable to investigate the interaction between guidance and adaptive control, and to determine how the adaptation mechanism performs with guidance in the loop.

2. An analysis was performed to determine the effects of uncertainties in the atmosphere as well as the vehicle inertias and aerodynamic coefficients on the performance of a controller. An extension to this work could include the investigation of the effects of uncertainties in the control influence matrix.

3. This thesis developed two adaptive control systems that were tuned to minimize the control input signal. This signal was continuous and within the maximum possible output of three RCS jets fired at a given time. An important extension to this work is the study of discrete control effectors with an adaptive control system. The simulation created for this work could be extended by adding control allocation logic for the use of reaction control system jets.

4. The entry simulation used for this research uses the bank angle as a control degree-of-freedom to steer the lift vector about the velocity vector. By steering the lift vector, the rte of descent of the vehicle as well as the downrange and crossrange distances can be controlled. An additional control degree-of-freedom could be introduced by varying the angle-of-attack. It is recommended that the benefits of this additional degree-of-freedom are investigated.

5. In the past, ballistic entry vehicles have used phase plane controllers. In order to quantify the benefits of an adaptive control system more specifically, it would be valuable to make a comparison between a phase plane controller and an adaptive system. A trade study between tracking performance levels and implementation issues for each type of controller would be valuable.

6. Certification of flight control systems is a difficult task. If an adaptive control system were to be implemented on a real flight vehicle, it will most likely require a different type of certification methodology than the ones used now. It would be very helpful to study what issues might arise when certifying an adaptive system for flight and to what extent the designer can trust the adaptation mechanism without setting bounds or implementing constraints on certain parameters.

REFERENCES

[1] W. Schneider, C. Graves, J. LeBeau, D. Curry, M. Munk *et al.*, "Mars combo lander design study," 1998, (NASA internal document).

[2] C. Justus, A. Duvall, and D. Johnson, "Mars global reference atmosphere model and database for mission design," NASA Marshall Space Flight Center, Tech. Rep., 2001.

[3] D. A. Spencer and R. D. Braun, "Mars pathfinder atmospheric entry - trajectory design and dispersion analysis," *Journal of Spacecraft and Rockets*, vol. 33, no. 5, pp. 670–676, 1996.

[4] J. Slotine and W. Li, *Applied Nonlinear Control*. Upper Saddle River, NJ: Prentice Hall, 1991.

[5] C. Graves, "Entry configurations and performance comparisons for the mars smart lander," in *Proceedings of the AIAA Guidance, Navigation, and Control Conference and Exhibit*, Monterey, CA, August 5-8, 2002.

[6] D. Kass, "Analysis of atmospheric mesoscale models for entry, descent and landing," in *Proceedings of the Sixth International Conference on Mars*, Pasadena, CA, July 20-25, 2003.

[7] A. Seiff and D. Kirk, "Structure of the atmosphere of mars at summer mid-latitudes," *Journal of Geophysical Research*, vol. 82, no. 28, pp. 4364–4378, September 1977.

[8] J. Shierman, D. Ward, J. Hull, N. Ghandi, M. Oppenheimer *et al.*, "Integrated adaptive guidance and control for re-entry vehicles with flight-test results," *Jour-*

nal of Guidance, Control, and Dynamics, vol. 27, no. 6, pp. 975–988, November - December 2004.

[9] S. Graybeal and K. Kranzusch, "Entry abort determination using non-adaptive neural network for mars precision landers," in *Proceedings of the AIAA Guidance, Navigation, and Control Conference and Exhibit*, San Francisco, CA, August 15-18, 2005.

[10] P. Desai and P. Knocke, "Mars exploration rovers entry, descent, and landing trajectory analysis," in *Proceedings of the AIAA/AAS Astrodynamics Specialist Conference and Exhibit*, Providence, RI, August 16-19, 2004.

[11] E. Wong and J. Masciarelli, "Autonomous guidance and control design for hazard avoidance and safe landing on mars," in *Proceedings of the AIAA Atmospheric Flight Mechanics Conference and Exhibit*, Monterey, CA, August 5-8, 2002.

[12] K. Narendra and A. Annaswamy, *Stable Adaptive Systems*. Mineola, NY: Dover Publications, 2005.

[13] M. R. Akella, "Structured adaptive model control: Theory and applications to trajectory tracking in aerospace systems," Ph.D. dissertation, Aerospace Engineering, Texas A&M University, College Station, TX, 1999.

[14] A. Seiff, "Mars atmospheric winds indicated by motion of the viking landers during parachute descent," *Journal of Geophysical Research*, vol. 98, no. E4, pp. 7461–7474, April 1993.

[15] F. Ferri, P. Smith, M. Lemmon, and N. Renno, "Dust devils as observed by mars pathfinder," *Journal of Geophysical Research*, vol. 108, no. E12, pp. 7–1 – 7–10, December 2003.

[16] M. P. Golombek, J. A. Grant, T. J. Parker, D. M. Kass, J. A. Crisp *et al.*, "Selection of the mars exploration rover landing sites," *Journal of Geophysical Research, Planets*, vol. 108, no. E12, pp. ROV 13–1 to ROV 13–48, December 2003.

[17] G. Carman, D. Ives, and D. Geller, "Apollo-derived mars precision lander guidance," in *Proceedings of the AIAA Atmospheric Flight Mechanics Conference and Exhibit*, Boston, MA, August 10-12, 1998.

[18] G. Mendeck and G. Carman, "Guidance design for mars smart landers using the entry terminal point controller," in *Proceedings of the AIAA Atmospheric Flight Mechanics Conference and Exhibit*, Monterey, CA, August 5-8, 2002.

[19] K. Dutton, "Optimal control theory determination of feasible return-to-launch-site aborts for the hl-20 personnel launch system vehicle," NASA, Tech. Rep. 3449, July 1994.

[20] P. Read, M. Collins, F. Forget, R. Fournier, F. Hourdin *et al.*, "A gcm climate database for mars: For mission planning and for scientific studies," *Advanced Space Research*, vol. 19, no. 8, pp. 1213–1222, 1997.

[21] K. Astrom and B. Wittenmark, *Adaptive Control*, 2nd ed. Upper Saddle River, NJ: Prentice Hall, 1994.

[22] S. Bhattacharya and L. Chapellat, *Robust Control: The Parametric Approach*. Prentice Hall, Upper Saddle River, NJ, 1995.

[23] "Fssr oi-27 space shuttle entry flight control system," January 1998, (NASA Technical Specifications).

[24] P. A. Iannou and J. Sun, *Stable and Robust Adaptive Control*. Prentice Hall, Upper Saddle River, NJ, 1995.

[25] M. Tandale and J. Valasek, "Adaptive dynamic inversion control with actuator saturation constraints applied to tracking spacecraft maneuvers," *Journal of Astronautical Sciences*, vol. 52, pp. 671–680, November - December 2005.

[26] ——, "Fault tolerant structured model inversion control," *Journal of Guidance, Control, and Dynamics*, vol. 29, no. 3, pp. 635–642, June 2006.

[27] M. Akella, J. Junkins, and H. Shaub, "Adaptive control of nonlinear attitude motions realizing linear closed-loop dynamics," in *Proceedings of the American Control Conference*, San Diego, CA, June 2-4, 1999.

[28] K. Subbarao, J. Junkins, and M. Steinberg, "Structured adaptive model inversion applied to tracking aggressive aircraft maneuvers," in *Proceedings of the AIAA Guidance, Navigation, and Controls Conference and Exhibit*, Montreal, Canada, August 6-9, 2001.

[29] M. Tandale and J. Valasek, "Adaptive dynamic inversion control with actuator saturation constraints applied to tracking spacecraft maneuvers," in *Proceedings of the 6th International Conference on Dynamics and Control of Systems and Structures in Space*, 2004.

[30] H. Shaub and J. Junkins, *Analytical Mechanics of Space Systems*. Reston, VA: American Institute of Aeronautics and Astronautics, Inc., 2003.

VITA

Carolina Isabel Restrepo was born in Texas and raised in Colombia and Bolivia. She began her undergraduate studies at Texas A&M University in January 2001 and received her Bachelor of Science Degree in Aerospace Engineering on December 2005. In January 2006, Carolina began her graduate studies under the advisement of Dr. John Valasek at Texas A&M. This thesis is the culmination of her graduate research and has been submitted in partial fulfillment of the requirements for a Master of Science degree in Aerospace Engineering. Ms. Restrepo worked at the NASA Johnson Space Center as a co-operative education student during her undergraduate and graduate years.

Contact Information: Dr. John Valasek, Department of Aerospace Engineering, Texas A&M University, College Station, TX 77843.